

NANOMATERIALS FOR HIGH EFFICIENCY MEMBRANE DISTILLATION

by

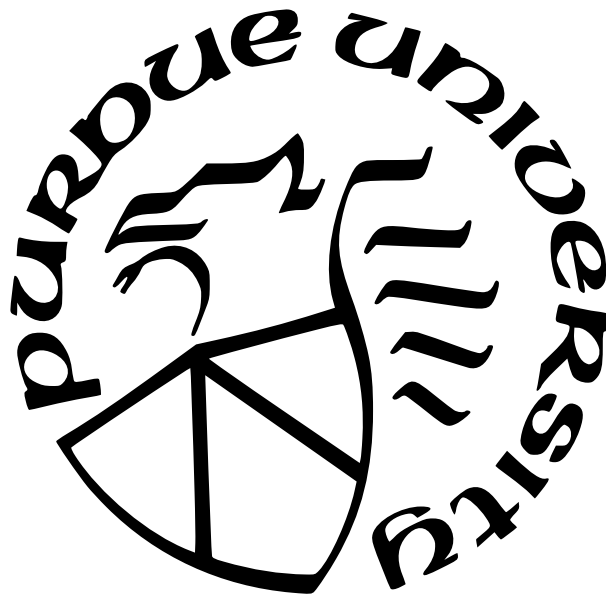
Harsharaj Birendrasingh Parmar

A Thesis

Submitted to the Faculty of Purdue University

In Partial Fulfillment of the Requirements for the degree of

Master of Science in Mechanical Engineering



School of Mechanical Engineering

West Lafayette, Indiana

May 2021

**THE PURDUE UNIVERSITY GRADUATE SCHOOL
STATEMENT OF COMMITTEE APPROVAL**

Dr. David Warsinger, Chair
School of Mechanical Engineering

Dr. Justin Weibel
School of Mechanical Engineering

Dr. Amy Marconnet
School of Mechanical Engineering

Approved by:
Dr. Nicole L. Key

To my parents for their unconditional love and support.

ACKNOWLEDGMENTS

I would like to pay high regards to my supervisor Prof. David M Warsinger for his valuable insights and guidance in defining my research pathway. I would also like to thank my co-authors and lab mates Mr. Hamid Fattahi Juybari and Mr. Yashwant Sawaisingh Yogi for their efforts in producing experimental results to support my modelling studies.

I would like to acknowledge Convergence Industry B.V. for providing the membrane distillation experimental setup and Porous Materials Inc. (PMI) for providing the membrane characterization instruments. In particular, I would like to thank Mr. Rishav Roy, Purdue University for helping with the contact angle measurements and condensation imaging, Mr. Timothy Simon, Purdue University for providing purchasing information on nanofluids, and Ms. Yuhang Fang, Purdue University for assisting in SEM characterization for the nanofluids chapter.

I am grateful to my team of undergrads - Mr. Ali Alshubbar, Purdue University for assisting in the optimal porous condenser calculations, Mr. Cameron Phillip Harvey, Purdue University for his relentless pursuits in modelling the transport at low gap pressures using CFD, Ms. Katherine Leigh Young, Purdue University for helping with the artwork and content edits, Mr. Prashant Suresh Menon, Purdue University and Mr. Ryan Madhu Jacob, Purdue University for carrying out the DLS characterization of nanofluids. I also thank the other group members who have had direct or indirect contributions in facilitating this work.

TABLE OF CONTENTS

LIST OF TABLES	8
LIST OF FIGURES	9
LIST OF SYMBOLS	14
ABBREVIATIONS	16
ABSTRACT	17
1 INTRODUCTION	18
1.1 The need for thermal desalination	18
1.2 Membrane distillation	19
1.3 Benefits of channel heat transfer enhancements	19
1.4 Motivation for energy efficient high salinity desalination	20
1.5 Outline of contributions	20
2 MODELLING THE PERFORMANCE OF MEMBRANE DISTILLATION	22
2.1 Modelling membrane distillation systems	22
2.1.1 Hot feed side equations	22
2.1.2 Gap transport equations	24
2.1.3 Cold feed side equations	25
2.2 Efficiency metrics in membrane distillation	25
2.2.1 First law efficiency metric: GOR	25
2.2.2 Thermal efficiency	25
2.2.3 Second law efficiency	26
3 NANOFUIDS IMPROVE ENERGY EFFICIENCY OF MEMBRANE DISTIL- LATION	29
3.1 Heat transfer enhancements via nanofluids	29
3.2 Materials and Methods	30

3.2.1	Experimental methods	31
3.2.2	Numerical modelling	33
	Nanofluid thermal conductivity relations	33
	Nanofluid properties: density, specific heat and viscosity	35
3.3	Results and Discussion	36
3.3.1	Modelled thermal conductivity enhancements from nanofluids	37
3.3.2	Relative energy efficiency of various MD configurations	38
3.3.3	Benchmark efficiency metrics for conductive gap MD systems	40
3.3.4	Particle dispersion after sonication of nanofluids	40
3.3.5	Particle size analysis with dynamic light scattering	42
3.3.6	Effects of nanofluids on membrane fouling and hydrophobicity	42
4	SLIPPERY LIQUID INFUSED POROUS SURFACES (SLIPS) FOR HIGH EFFICIENCY AIR GAP MEMBRANE DISTILLATION	46
4.1	Background	46
4.1.1	Flooding in air gap membrane distillation	46
4.1.2	Novel condensation regime on SLIPS	46
4.2	Modeling of SLIPS surfaces in MD	47
4.2.1	Overview	47
4.2.2	Dropwise condensation	48
4.2.3	Numerical Methodology	49
4.3	Results and Discussions	50
4.3.1	Efficiency validation for baseline AGMD	51
4.3.2	Efficiency validation for SLIPS AGMD	51
4.3.3	Practical performance metrics	53
5	POROUS CONDENSERS IN MEMBRANE DISTILLATION FOR EFFICIENT HIGH SALINITY DESALINATION	55
5.1	Heat transfer enhancements using porous condensers	55
5.2	Materials and Methods	56
5.2.1	Experimental methods	56

5.2.2	Numerical methodology	57
5.2.3	Heat and mass transfer through porous condensers	57
5.3	Results and Discussions	58
5.3.1	Experimental thermal efficiency and permeate production	59
5.3.2	Performance comparison of MD configurations	60
5.3.3	Optimal condenser thickness for seawater desalination	61
5.3.4	Condensation images at atmospheric conditions	61
6	CONCLUSIONS AND FUTURE WORK	63
6.1	Nanofluids for energy efficient desalination	63
6.2	Novel condensation surfaces enhance high salinity desalination	63
6.3	Future work	64
	REFERENCES	66
A	NANOFUID MODEL SYSTEM PARAMETERS	79
B	SLIPS MODEL SYSTEM PARAMETERS	80
C	POROUS CONDENSER MODEL SYSTEM PARAMETERS	81

LIST OF TABLES

3.1	Copper oxide (CuO) and carbon nanotube (MWCNT) nanofluids characterized for MD, with details on their concentration and sonication duration	32
A.1	System parameters used in the numerical model for nanofluids in membrane distillation	79
B.1	System parameters used in the numerical model for SLIPS in membrane distillation	80
C.1	System parameters used in the numerical model for porous condensers in membrane distillation	81

LIST OF FIGURES

1.1	Prominent thermal desalination technologies with a brief outline of the heat and mass transfers involved in their operation. Top row starting from left - steam generator, solar still, membrane distillation. Bottom row starting from left - multistage flashing, multieffect distillation, humidification dehumidification [2].	19
2.1	Computational element of the MD model: A graphical representation of the various heat and mass transfers involved in an air gap membrane distillation system. The heat transfer across the membrane is governed by conduction and vapor transport. The feed, permeate mass flow rates and enthalpy are shown along with the variation of temperature over the width of the module.	23
2.2	Heat and mass transfer in membrane distillation: Heat input and heat recovery in the module, showing key parameters to calculate the thermal efficiency of membrane distillation, η_{th} . The heat transfer rates shown are those that define η_{th} , and the feed temperatures shown can be used to easily calculate the overall thermal efficiency η_{th} , or the heat transfer effectiveness ϵ for the system [1], [2]. .	27
2.3	Least heat of separation: Least heat in kWh/m ³ required to obtain freshwater as a function of the feed inlet salinity and desired recovery ratio from the desalination process. Gibbs free energy is used to calculate the theoretical least heat and property evaluations are carried out in the salinity range of 0–120 g/kg [2].	28
3.1	Heat transfer enhancement using nanofluids: The dominant modes of heat transfer enhancement using copper oxide nanoparticles and carbon nanotubes in a distilled water basefluid. Brownian motion and the associated micro-mixing is the dominant mechanism for improved heat transfer in copper oxide nanofluid. Van der Waals interaction of carbon nanotubes results in a substantially high axial heat conduction through phonon resonance across the fluid.	30
3.2	Preparation of nanofluids: Nanofluid preparation using sodium dodecylbenzenesulfonate (SDBS) surfactant and sonication. Copper oxide nanoparticles are shown as orange spheres and multi-walled carbon nanotubes are represented by gray stands (top, middle).	32
3.3	Nanofluids in membrane distillation: Membrane Distillation (MD) schematic with the addition of nanofluids. Three different configurations can be made by modifying the gap properties between the membrane and condenser plate. Air gap membrane distillation (AGMD), shown above, introduces a stagnant air medium in the gap region, permeate gap membrane distillation (PGMD) is obtained when the gap is flooded with water and finally conductive gap membrane distillation (CGMD) has conductive spacers stacked up in the gap.	34

3.4	<p>Property variations in nanofluids: A) Variation of thermal conductivity for CuO-Water and Carbon Nanotube (MWCNT)-Water nanofluid by particle volume fraction, where contributions to thermal conductivity from Brownian motion are shown by shaded regions. B) Property changes relative to seawater in the feed at various nanoparticle concentrations, including viscosity μ, density ρ, heat capacity c_p and conductivity k. Properties were evaluated at an average temperature of the MD system (55°C). Brownian motion and the interaction of particles significantly increases the nanofluid thermal conductivity compared to seawater (0.668 [W/mK]).</p>	37
3.5	<p>Nanofluid improvements by MD configuration: A), B) Relative enhancement of energy efficiency (GOR) with nanoparticle volume fraction for AGMD, PGMD and CGMD configurations. AGMD and PGMD configurations showed lower enhancements due to a dominant gap heat transfer resistance. Energy efficiency (GOR) vs gap thermal conductivity: C), D) for a CGMD configuration using nanofluids in the feed channels. Nanoparticle concentration was varied for copper oxide and carbon nanotubes along with changes to the gap thermal conductivity. A point for water flooded gap enhancement (PGMD) is also shown for comparison. The optimal performance does not change much for copper oxide nanoparticles after a concentration of roughly 0.7%, whereas carbon nanotubes show more continuous improvements. The difference is likely due to separate thermal mechanisms being dominant, as copper oxide nanofluids are highly dependant on Brownian motion, which is reduced by agglomeration at higher nanofluid concentrations.</p>	39
3.6	<p>Sonication of nanofluids: Effects of sonication on the clustering of nanoparticles in 0.001% nanofluid with 0.005% SDBS solution samples dried on a glass plate. Carbon nanotubes showed massive agglomeration A) after magnetic stirring and were widely dispersed after 2 hours of sonication B). The length of nanotube agglomerates stayed above 500 nm even after sonication due to their strong axial interaction forces. These long, surfactant stabilized nanotube strands reduce the Brownian motion but are very effective in static conduction across the fluid. Copper oxide clusters of the order of 1 μm C) were broken down to characteristic size scales smaller than 200 nm D), which effectively contributed to thermal conductivity enhancements from their Brownian motion. Nanofluid particle size vs sonication, via dynamic light scattering: Variation of average particle size of carbon nanotubes E) and copper oxide F) with sonication duration for two different concentrations of SDBS surfactant (0.05% and 0.005%). The SDBS surfactant showed reduced effectiveness above a concentration of 0.01% (yellow, 0.05% SDBS). Particle sizes increased abruptly after longer sonication durations for 0.05% SDBS concentration, due to the development of stable air bubbles in the solution which inhibited the nanoparticle cluster breakage.</p>	41

3.7	Macroscopic images of PTFE membrane after fouling tests with MWCNT and copper oxide nanofluids. Part A) shows a clean PTFE membrane and B) , C) show the fouled counterparts, flushed with water for 5 minutes to remove the loosely adhered particles. Carbon nanotubes show substantial membrane fouling at the macroscale B) due to their higher particle density in comparison to copper oxide nanoparticles C)	43
3.8	Membrane fouling from nanofluids: SEM micrographs showing the fouling of a PTFE membrane using 0.1% nanofluid solutions. Dark black spots in part B) show significant clustering of carbon nanotubes on the membrane surface and interactions with the membrane fibres at the microscale E) . SDBS surfactant reduces the surface tension of the feed, decreasing the membrane hydrophobicity and allowing nanoparticles to interact with the membrane. Nanotubes have a very high number density (number of particles per unit volume) and as a result, showed extensive membrane fouling. Negligible membrane fouling is observed using copper oxide with very few micrometer scale agglomerates C) , F) interacting with the membrane fibres. Energy dispersive x-ray spectroscopy (EDS) was used to identify the copper oxide nanoparticles in the membrane.	44
3.9	Hydrophobicity comparison of the fouled membranes: Static contact angle of water on a clean PTFE membrane and two nanofluid fouling tested PTFE membrane samples. The reduction in membrane hydrophobicity is nearly equal after using CuO-Water and MWCNT-Water nanofluids in the feed channel, since they have the same SDBS surfactant concentration. The carbon nanotube fouled membrane sample shows a relatively higher variation in measurements due to the uneven membrane surface caused by significant nanotube deposition.	45
4.1	Condensation regimes in membrane distillation: Schematic of an air gap membrane distillation system showing film-wise condensation on unstructured copper surface (top), droplet shedding on SLIPS and jumping droplet condensation on superhydrophobic surfaces (below). Temperature variations across the membrane and air gap are described along with the dominant heat and mass transfer resistances in the system [17].	48
4.2	Thermal efficiency validation for film-wise condensation: Comparison of the experimental and modeling results for film-wise condensation inside a lab scale membrane distillation module. The increase in the hot feed side temperature results in a higher driving force for vapor production across the membrane. The enhancements in vapor production follow an exponential trend with temperature and outweigh the conduction losses across the membrane, thereby improving the thermal efficiency [17].	52

4.3	Thermal efficiency validation for SLIPS: Comparison of the experimental and modeling results for SLIPS condensation inside a lab scale membrane distillation module. Minor deviations in thermal efficiency were observed at lower feed temperatures due to the droplet entrapment in the mesh spacers at such low permeate flux values. The droplets effectively increased the thermal conductivity of the gap and resulted in higher conduction losses and compromised thermal efficiency compared to the model results [17].	52
4.4	SLIPS performance improvement: Energy efficiency and permeate production with module length for SLIPS and film-wise condensation at various salinities and matching air gap sizes. Efficiency curves were plotted at the optimal gap size at each salinity for SLIPS and the enhancements were shaded for clarity. For film-wise condensation, frontiers at 5 and 35 g/kg salinities had been plotted at the gap sizes that prevent flooding (0.1 and 0.14 mm respectively) whereas for other salinities gap size was identical to SLIPS. Module length was varied from 0.5 to 30 m to properly capture the GOR value peaks for the considered salinity range of 5–105 g/kg [17].	54
5.1	Porous condensers in membrane distillation: Experimental setup for a PC-AGMD system showing the porous copper condenser inside the membrane distillation module and an enlarged view of the porous structure. Schematic showing the heat and mass transfer across a PC-AGMD and AGMD system. . .	56
5.2	Experimental performance comparison of PC-AGMD and AGMD: Comparison of the permeate flux and thermal efficiency across different MD configurations with variations in the top temperature of the feed at seawater salinity. The average flux improvement with the porous condenser was 96.5%, and the thermal efficiency enhancement was 31.7%. Porous condensers are very effective in water transport across the air gap due to their wicking properties and result in dramatic permeate flux enhancements. Flux improvements result in increased latent heat recovery which effectively translates to higher energy efficiency.	59
5.3	Relative performance comparison of PC-AGMD with leading MD configurations: GOR-flux frontiers across different MD configurations with variations in the module length at seawater salt concentration and high salinity (175 g/kg). PC-AGMD outperforms AGMD and PGMD due to the improved conductive heat transfer across the gap and increased active surface area for vapor condensation. CGMD performs the best at seawater salt concentrations but is significantly compromised at high salinities where PC-AGMD provides the best performance. The gap size is maintained at 3 mm across all the configurations and the rest of the modeling conditions are mentioned in the Appendix C.	60

5.4	Optimized porous condenser thickness: Optimal porous condenser thickness with increasing module length at various wick permeabilities. Increasing the permeability of the condenser results in more effective droplet removal, and thus allows the operation at smaller gap sizes. Lowering the permeability promotes an early incipience of flooding in the condenser and inhibits the energy efficiency of the PC-AGMD configuration.	61
5.5	Condensation imaging of porous condensers: Open air condensation imaging of porous condensers at the beginning of droplet nucleation and after coalescence of smaller droplets to larger sizes (shown by red circles). Numerous tiny droplets are formed at the initial phase on the surface of the porous condenser indicating the availability of nucleation sites. Droplet coalescence does not flood the pores of the condenser and the large droplets are shed easily from their nucleation sites by gravity.	62

LIST OF SYMBOLS

Roman symbols

k	thermal conductivity, W/m·K
c_p	specific heat capacity, J/kg·K
T	temperature, K
D	average particle diameter, m
\dot{m}	mass flow rate, kg/s
h_{fg}	enthalpy of vaporization, J/kg
\dot{Q}	heat transfer rate, W
h	heat transfer coefficient, W/m ² ·K
r_d	departing droplet radius, m
r_i	effective length equating conduction and interfacial resistance, m
r_t	minimum droplet radius, m
g	acceleration due to gravity, m/s ²
g	gibbs free energy, J/kg
R_g	specific ideal gas constant
D_{w-a}	diffusion coefficient of water vapor in air
J_m	vapor flux across the membrane, kg/m ² ·s
M_w	molecular weight of water, kg
c_a	molar concentration of air, mol/m ³
d_{gap}	gap size in membrane distillation, m
x	mole fraction
w	width of the condenser, m
\dot{W}_{least}	least work of separation, W

Greek symbols

α_p	particle volume fraction
β	particle motion modification
ρ	density, kg/m ³
κ	Boltzmann constant

μ	viscosity, kg/m·s
θ	contact angle
σ	surface tension, N/m
γ	heat capacity ratio
δ	film thickness, m
δ_c	thickness of the porous condenser, m
η_{th}	thermal efficiency
η_{II}	second law efficiency

Subscripts

bf	basefluid
brownian	Brownian motion enhancement
eff	effective property of nanofluid
gap	gap between membrane and condenser plate
max	maximum
min	minimum
nf	nanofluid
per	permeate
p	particle
static	static thermal conductivity enhancement
a	air
i	condensate film and air gap interface
m	membrane
b	brine
sw	seawater
vap	evaporation
cond	conduction

ABBREVIATIONS

MD	membrane distillation
AGMD	air gap membrane distillation
PGMD	permeate gap membrane distillation
CGMD	conductive gap membrane distillation
PC-AGMD	porous condenser air gap membrane distillation
VMD	vacuum membrane distillation
VAGMD	vacuum air gap membrane distillation
GOR	gained output ratio
RR	recovery ratio
LMH	litres per meter square hour
MWCNT	multi-walled carbon nanotubes
CuO	copper oxide
PTFE	polytetrafluoroethylene
SDBS	sodium dodecylbenzene sulfonate
DLS	dynamic light scattering
SEM	scanning electron microscopy
EDS	energy dispersive x-ray spectroscopy
SLIPS	slippery liquid infused porous surfaces
EES	engineering equation solver

ABSTRACT

Thermal desalination of high salinity water resources is crucial for increasing freshwater supply, but efficiency enhancements are badly needed. Nanomaterial enhancements and novel condensation regimes offer enormous potential for improving promising technologies like membrane distillation (MD). In this work, we first examined nanofluids for MD, including the role of nanoscale physics, and model system-level energy efficiency enhancements. Our model included the dominant micro-mixing from Brownian motion in fine particle nanofluids (copper oxide) and the unusually high axial conduction from phonon resonance through Van der Waals interaction in carbon nanotube nanofluids. Carbon nanotubes resulted in a consistent, wide range of improvements; while copper oxide particles showcased diminishing returns after a concentration of 0.7%, where Brownian motion effects reduced. However, the enhancements at higher concentrations from liquid layering around nanoparticles were impractical in MD, since the related high surfactant levels compromised the membrane hydrophobicity and promoted fouling. Dilute solutions of metallic nanofluids can be actively integrated to enhance the performance of MD, whereas stronger nanofluid solutions should be limited to heat exchangers that supply thermal energy to MD systems. We then investigated slippery liquid infused porous surfaces (SLIPS) for enhanced condensation rates in MD. Dropwise condensation heat transfer was modelled considering the effects of the departing, minimum droplet radii and the interfacial thermal resistances. Effective droplet shedding from these surfaces led to an experimental thermal efficiency of 95%. Alternatively, porous condensers with superior wicking properties and conductive heat transfer offered a robust solution to high salinity desalination. We modelled the onset of flooding in porous condensers using Darcy's law for porous media, including the effects of the condenser permeability and determined the optimal condenser thickness at varying system length scales. The increased active area of condensation resulted in a significant enhancement (96.5%) in permeate production and 31.7% improvement in experimental thermal efficiency. However, porous condensers were only compatible with flat plate module designs limiting their practicality.

1. INTRODUCTION

Disclaimer: Contents of this chapter are parts of submitted journal publications [1], [2].

1.1 The need for thermal desalination

Freshwater resources are being substantially overexploited around the world to meet rising water demand. The desalination of alternative sources like seawater, and brackish water presents a possible solution [3]–[5], but the concentration to highly saline feeds tends to be energy intensive [6]–[9]. Commercial pressure-driven desalination processes like reverse osmosis are impractical at high salt concentrations [10]–[12] and thus the general consensus is that improvements of thermal desalination technologies (prominent ones are shown in Figure 1.1) are needed for high salinity and high water recovery applications. Thermal technologies like solar evaporators, solar stills are plagued by low water recoveries, while large scale processes like multistage flashing and multieffect distillation require a huge amount of thermal energy. Membrane distillation (MD) operates between these two extremes in the sense that it utilizes low temperature heat and exhibits easy integration with renewable energy sources. However, the inherent phase change in MD leads to proportionally high energy costs, which often constitute about two-thirds of the total operating expense [13]. Optimizing the heat and mass transfer in MD is therefore crucial because even minor improvements in efficiency can reflect as major industrial cost savings [14], [15].

Over the years, fundamental studies on improving the transport physics in membrane distillation have led to the introduction of novel configurations. However, recent investigations on enhancements in membrane distillation have failed to characterize their performance across diverse system scales and have focused on specific configurations. In this work, we present a comprehensive analysis of the heat and mass transfer enhancements across all the leading MD configurations using novel working fluids [16] and effective condensation regimes [17], [18] for optimal latent heat recovery. A methodological approach is used here to evaluate the performance improvements in a lab-scale module, which are then extrapolated to practical MD systems using a sophisticated numerical model capturing the complex transport physics in membrane distillation.

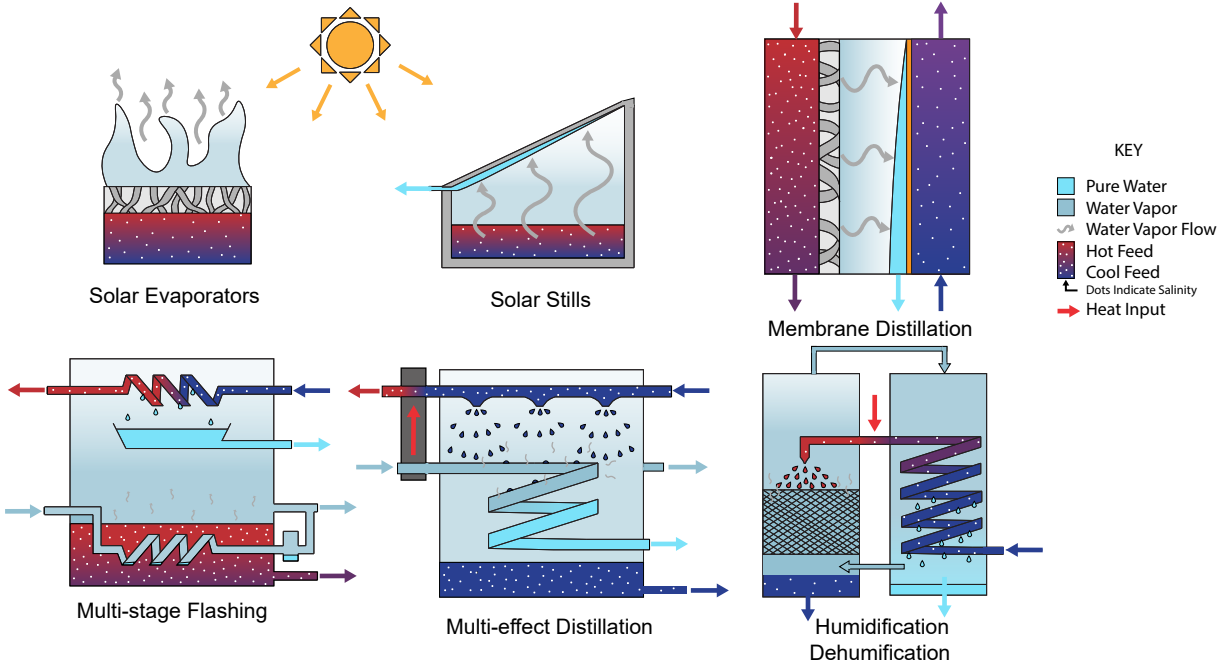


Figure 1.1. Prominent thermal desalination technologies with a brief outline of the heat and mass transfers involved in their operation. Top row starting from left - steam generator, solar still, membrane distillation. Bottom row starting from left - multistage flashing, multieffect distillation, humidification dehumidification [2].

1.2 Membrane distillation

One of the emerging thermal desalination processes - membrane distillation (MD) has shown the ability to retain performance at high salinities [19], [20]. From a broad perspective, MD systems reveal a close resemblance to counterflow heat exchangers with an added membrane between the two channels [21]. The hydrophobic membrane prevents the permeation of non volatile salts [22] to separate the hot feed stream (brine) and the cold distillate stream (pure water). Temperature difference between the two sides of the membrane results in a vapor pressure gradient that drives the desalination [23], [24].

1.3 Benefits of channel heat transfer enhancements

The temperature difference across MD membranes governs the pure water flux but also leads to significant heat conduction losses [25]. In order to eliminate these losses, air gap

membrane distillation (AGMD) [26]–[28] introduces a thick air layer between the membrane and condensing surface. The additional MD configurations are classified by the properties of the gap between the membrane and condensing surface, like permeate gap membrane distillation (PGMD) [29]–[31] where the gap is flooded with water and conductive gap membrane distillation (CGMD) with high gap conductance [32], [33]. In all these configurations, the vapor condenses within the gap and effective phase change regimes have demonstrated significant performance enhancements [17], [18], [34]. However, these modifications are often beneficial when flux stability is achieved from improved feed channel heat transfer using turbulence promoters [35] and corrugations [36] but such channel structures are optimized for specific flow conditions. As a result, methods that can preserve the feed heat transfer enhancements across varied operating conditions are desirable.

1.4 Motivation for energy efficient high salinity desalination

Gap based MD configurations like permeate gap membrane distillation (PGMD) where the gap is flooded with water, and conductive gap membrane distillation (CGMD) with conductive mesh spacers in the gap, have led to reduced conduction losses [33], [37]. Notably, these configurations enhance the performance of MD at seawater salinities (35 g/kg) but are compromised at high salt concentrations [12]. On the other hand, air gap membrane distillation (AGMD) systems show consistent performance across the entire salinity range [26], [38] and are further improved by novel working fluids [16] and condensation regimes in the gap [17], [27]. These regimes result in effective permeate removal after condensation, but the air gap still poses a significant resistance to vapor transport limiting their performance enhancements [34]. As a result, there is a need to improve the vapor transport across the gap in AGMD using intricate structures that exhibit superior droplet shedding along with efficient heat transfer characteristics.

1.5 Outline of contributions

Heat transfer enhancements in the feed channels of MD have been previously obtained using geometrical modifications, but they are usually optimized for specific flow conditions.

Here, we modify the thermal conductivity of the fluid using nanoparticles to achieve uniform convective heat transfer improvements across diverse operating conditions. Moreover, understanding is lacking for dropwise condensation in AGMD at gap sizes below 2 mm and our work on SLIPS in AGMD investigates their performance in this gap regime. Finally, we introduce a novel porous wick in AGMD for superior heat and mass transfer at high salinities. Porous condensers have been implemented in solar desalination and heat exchangers and in this work we formally characterize the integration of porous wicks to membrane distillation.

In this work, we first outline the numerical methodology used to characterize MD systems and describe the various efficiency metrics in chapter 2. Thereafter, in chapter 3 we modify the intrinsic fluid properties using a novel nanofluid working medium in MD to result in uniform performance improvements. The heat transfer enhancements from nanofluids are modelled for different MD configurations and a comprehensive characterization of nanoparticle size, distribution is carried out to attain stable nanofluid solutions. The chapter concludes with a discussion on the effects of nanofluids on membrane fouling and reductions in hydrophobicity.

In chapters 4 and 5 we focus our attention towards high salinity desalination and improving the energy efficiency of air gap membrane distillation (AGMD). The chapter 4 marks the first comprehensive analysis of dropwise condensation on Slippery Liquid Infused Porous Surfaces (SLIPS) in membrane distillation to mitigate flooding issues in AGMD. SLIPS enabled AGMD systems are effective in droplet shedding and result in significant efficiency enhancements at practical system scales. Thereafter, in chapter 5 we introduce a novel and robust alternative for high salinity desalination using porous condensers with superior wicking properties in AGMD to achieve the best performance at high salt concentrations.

2. MODELLING THE PERFORMANCE OF MEMBRANE DISTILLATION

Disclaimer: Contents of this chapter are parts of submitted journal publications [1], [2].

2.1 Modelling membrane distillation systems

The complex heat and mass transfer physics in MD have been studied extensively through numerical models to understand the effects of system parameters on their flux [39], [40] and energy efficiency [19], [41], [42]. The modelling approach used here was based on the work from Summer et al. [43], and its details can be found in previous publications [12], [21], [26], [27], [33], [34].

In this section, we provide a high-level view of the model explaining the underlying physics and the approach used to quantify the transport processes. A computational element of the MD model discretized along the length of the module is shown in Figure 2.1, outlining the various mass flow rates, heat fluxes and temperatures. The governing equations are described for each control volume (hot feed side, gap, cold feed side) inside the discretized element and solved simultaneously using Engineering Equation Solver (EES) [44].

2.1.1 Hot feed side equations

Energy balance is carried out using a control volume in the hot feed channel to relate the heat transfer across the membrane and the bulk feed temperatures using,

$$\dot{Q}_{\text{out}} = \dot{m}_{\text{f,in}} h_{\text{f,in}} - \dot{m}_{\text{f,out}} h_{\text{f,out}}$$

where \dot{Q}_{out} is the net heat transfer out of the control volume, \dot{m} represents the mass flow rate and h is the specific enthalpy of the feed. The subscripts f,in and f,out refer to the feed entering and leaving the computational element respectively. The temperature

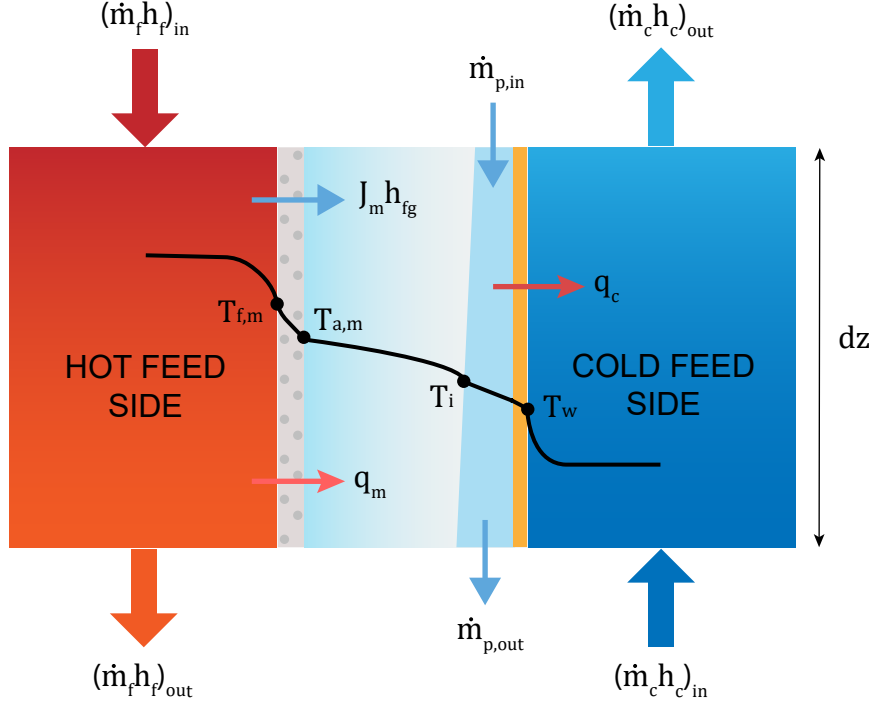


Figure 2.1. Computational element of the MD model: A graphical representation of the various heat and mass transfers involved in an air gap membrane distillation system. The heat transfer across the membrane is governed by conduction and vapor transport. The feed, permeate mass flow rates and enthalpy are shown along with the variation of temperature over the width of the module.

variations along the width of the channel are captured using boundary layers and governed by a convective heat transfer relation.

$$T_{f,b} - T_{f,m} = \frac{\dot{q}_{out}}{h_{t,f}}$$

where T represents temperature, \dot{q} represents the heat flux through the membrane and $h_{t,f}$ is the convective heat transfer coefficient obtained using well-validated heat transfer correlations for rectangular channels [45]. Here, the subscript f, b refers to the feed bulk and f, m refers to the surface of the membrane on the feed side. The water vapor flux across the membrane is related to the thermally induced vapor pressure gradient using the relation,

$$J_m = B (P_{f,m} - P_{a,m})$$

where J_m represents the vapor flux across the membrane, B represents the membrane permeability, $P_{f,m}$ is the vapor pressure near the membrane on the feed side and $P_{a,m}$ is the vapor pressure on the gap side.

2.1.2 Gap transport equations

The transport of water vapor across the gap in an air gap membrane distillation system (AGMD) is modelled using a binary diffusion equation as shown below,

$$\frac{J_m}{M_w} = \frac{c_a D_{w-a}}{d_{\text{gap}} - \delta} \ln \left(1 + \frac{x_i - x_{a,m}}{x_{a,m} - 1} \right)$$

where J_m is the vapor flux, M_w is the molecular weight of water, c_a is the molar concentration of air, d_{gap} is the gap size, δ the film thickness and x is the mole fraction of vapor in the gap. Here, subscript i represents the air-water interface and the a, m subscript represents the membrane-air interface. Moreover, the heat transfer through the air gap is captured using a convective-diffusive equation for temperature given as,

$$u \frac{dT}{dx} = \alpha \frac{d^2 T}{dx^2}$$

where u represents the convective velocity obtained using the mass flux J_m and α represents the thermal diffusivity of the air-vapor mixture. The film-wise condensation in AGMD is modelled using Nusselt's falling film theory on a flat plate and the increments in film thickness δ are related to the incoming vapor flux J_m .

In flooded gap configurations like permeate gap membrane distillation (PGMD) and conductive gap membrane distillation (CGMD), the vapor condenses at the gap-membrane interface and that simplifies the mass transport analysis. The heat transfer across the gap is then governed by conduction across the gap having a suitable thermal conductivity ($k_{\text{gap}} = 0.6$ for PGMD and 10 for CGMD).

2.1.3 Cold feed side equations

The analysis of the cold feed side is similar to that of the hot feed side but without any mass transfer across channel. Energy balance is carried out to relate the incoming heat with the increase in the bulk fluid temperature on the cold side. The temperature variations along the width of the channel are captured using boundary layers governed by a convective heat transfer relation.

2.2 Efficiency metrics in membrane distillation

2.2.1 First law efficiency metric: GOR

Perhaps the most common metric describing the efficiency of thermal desalination normalizes the specific energy consumption by the enthalpy of vaporization. This creates a dimensionless unit called the gained output ratio or GOR [1], [2].

$$\text{GOR} = \frac{\dot{m}_{\text{per}} h_{fg}}{\dot{Q}_h}$$

where \dot{m}_{per} [kg/s] represents the permeate flux output from MD system, h_{fg} [kJ/kg] is the latent heat of vaporization and \dot{Q}_h [kW] is the thermal energy input required. This metric can be thought of as a ratio of how many times better the process is compared to simply boiling and condensing without energy recovery. This metric may be identical to the "evaporation efficiency" (η_{evap}) often described in the solar evaporation field. Values can be as high as 20, but for systems without heat recovery, such as most direct solar evaporators or single-stage solar stills, the upper limit is 1 (100%).

2.2.2 Thermal efficiency

To understand the local level performance, a thermal efficiency, η_{th} , is used. This widely-applicable metric describes what fraction of incoming energy is kept to perform a process or sub-process. In thermal water production, the η_{th} of a particular step is useful for describing losses from individual parts of the process, such as heat losses to the environment, lost solar

energy from reflection, and conduction losses within a system. In the present context, this metric is most often used to describe heat transfer for the evaporation step in membrane distillation, and thus,

$$\eta_{th} = \frac{\dot{Q}_{\text{vap}}}{\dot{Q}_{\text{total}}}$$

where \dot{Q}_{vap} is the heat transfer from evaporation, and \dot{Q}_{total} equals the sum of evaporation \dot{Q}_{vap} , and various losses. Usually these losses are from conduction, \dot{Q}_{cond} , but for solar evaporation may include reflection of light. This thermal efficiency can be calculated easily from lab-scale experimental data with setups that have flowing feed water. Here, \dot{Q}_{vap} is simply a function of the pure water production rate \dot{m}_p , and enthalpy of evaporation, while the denominator can be described as a function total enthalpy removed by the feed stream (f), which can be described by the heat capacity c_p :

$$\eta_{th} = \frac{\dot{m}_p h_{fg}}{c_p (\dot{m}_{f,i} T_{f,i} - \dot{m}_{f,o} T_{f,o})}$$

where the temperatures are taken at the inlet (i) and outlet (o) of some portion of the feed side as shown in Figure 2.2.

2.2.3 Second law efficiency

By combining the first and second laws, one can analyze the available work, called exergy, between processes. This quantity is defined as the possible work that can be extracted from an energy source (e.g. sunlight or heat) that interacts with the environment. We call the least work for a separation process \dot{W}_{least} ;

$$\dot{W}_{\text{least}} = (g_{\text{per}} + g_b) - \frac{1}{RR} (g_{sw} - g_b)$$

where g is the Gibbs free energy, RR is the recovery ratio of pure water, and the subscripts are per for pure permeate, b for brine, and sw for seawater. The Gibbs free energy values are

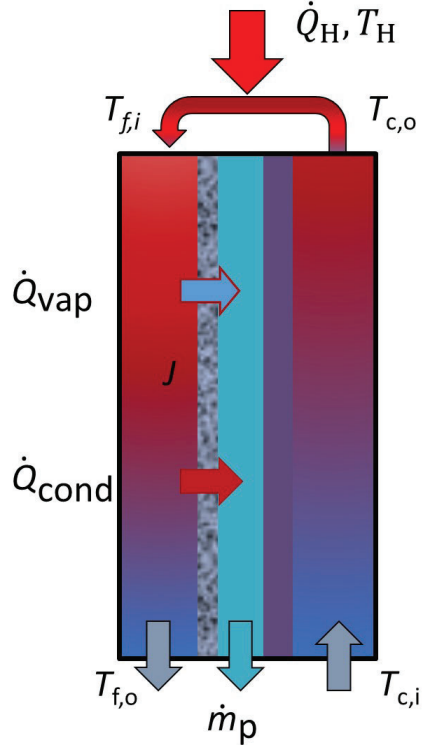


Figure 2.2. Heat and mass transfer in membrane distillation: Heat input and heat recovery in the module, showing key parameters to calculate the thermal efficiency of membrane distillation, η_{th} . The heat transfer rates shown are those that define η_{th} , and the feed temperatures shown can be used to easily calculate the overall thermal efficiency η_{th} , or the heat transfer effectiveness ϵ for the system [1], [2].

a function of the salt concentration. \dot{W}_{least} can be implemented with the actual work used by a real process, \dot{W}_{used} , to create a universal efficiency, called the 2nd law efficiency η_{II} ;

$$\eta_{II} = \frac{\dot{W}_{least}}{\dot{W}_{used}} = \frac{\text{Exergy change}}{\dot{W}_{used}} = \frac{\dot{Q}_{least}}{\dot{Q}_{used}}$$

this efficiency, η_{II} , is universal, as the exergy change can be calculated for any input to power the separation process, including heat, sunlight, fuels, or concentration differences. In membrane distillation, the second law efficiency is often expressed in terms of \dot{Q}_{least} and \dot{Q}_{used} and Figure 2.3 shows the variation of least heat of separation with changes in feed salinity and the desired recovery ratio of the desalination process.

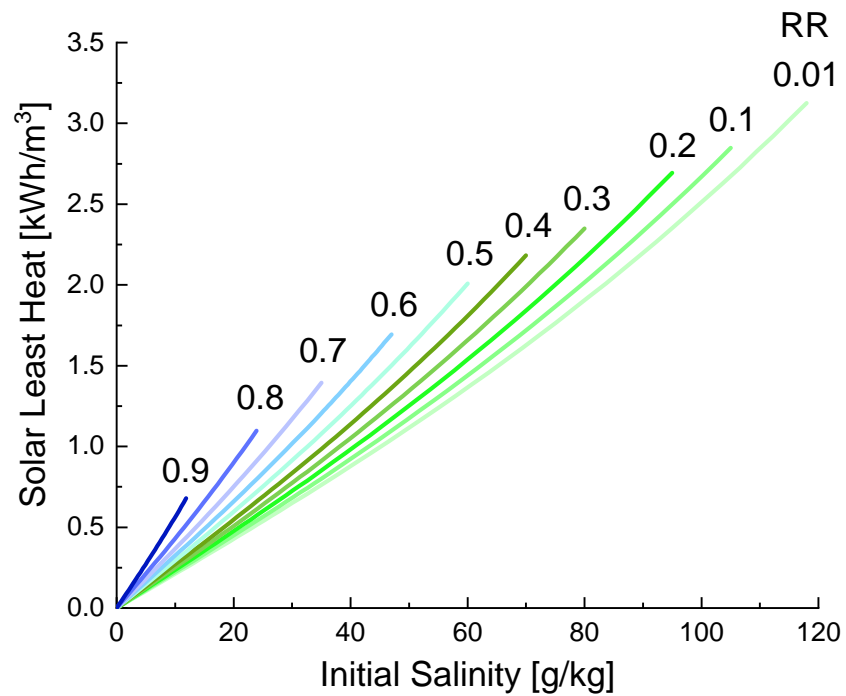


Figure 2.3. Least heat of separation: Least heat in kWh/m³ required to obtain freshwater as a function of the feed inlet salinity and desired recovery ratio from the desalination process. Gibbs free energy is used to calculate the theoretical least heat and property evaluations are carried out in the salinity range of 0–120 g/kg [2].

3. NANOFUIDS IMPROVE ENERGY EFFICIENCY OF MEMBRANE DISTILLATION

Disclaimer: Contents of this chapter are part of a submitted journal publication [16].

3.1 Heat transfer enhancements via nanofluids

Intrinsic fluid properties, notably thermal conductivity, directly affect the heat transfer and can be modified to attain performance improvements [46], [47]. To do so, high thermal conductivity nanofluids have been used in heat exchangers (15%-41% efficiency enhancements at concentrations of 0.1%-2%) [48]–[50], and their application is extended to MD here. Nanofluids are formed by suspending highly conductive nanoparticles (with size scales below 100 nm) in low conductivity base solutions [51]–[53]. Nanoparticles affect the thermal transport properties of the base fluid, improving thermal conductivity by mainly two mechanisms [54]. First, the static dispersion of particles results in simple concentration-based linear enhancements [55], [56], which fail to explain the significant conductivity increments observed in extremely dilute nanofluids [57]–[62]. These low concentration improvements are attributed to the second enhancement mechanism; the random motion of nanoparticles in the solution, also known as Brownian motion [63]. Randomly moving particles with high surface energy carry packets of fluid around, resulting in a phenomena called micro-mixing [64], [65]. Such micro-scale interactions in the fluid lead to a lower local temperature gradient for a given heat flux which, macroscopically translates to higher thermal conductivity. Nanoparticle-based thermal collectors have enhanced the productivity of solar stills and flashing desalination systems [66]–[71]. Additionally, immobilized nanoparticles in solar MD membranes effectively concentrated the solar radiation near the membrane to achieve higher permeate flux [72], [73]. However, these studies used nanoparticles to absorb thermal energy instead of explicitly improving the convective heat transfer using nanofluids.

To examine the performance of nanofluids in MD, here we presented a comprehensive energy efficiency analysis of the leading MD configurations (AGMD, PGMD and CGMD) with carbon nanotubes (MWCNT) and copper oxide (CuO) nanoparticles in the feed chan-

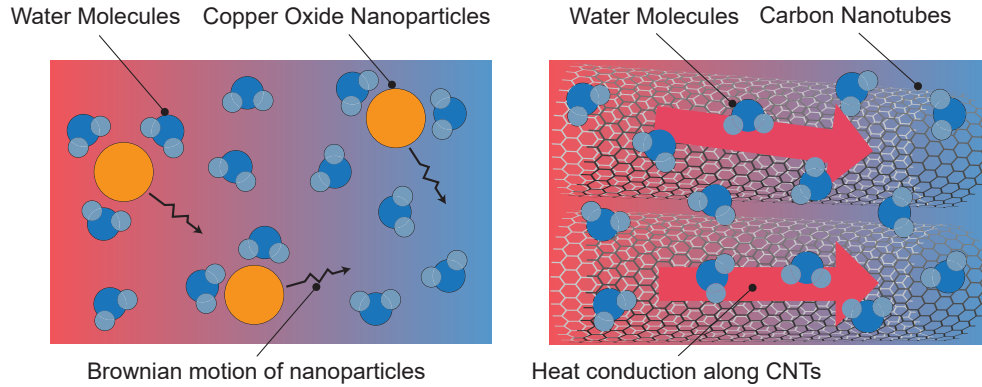


Figure 3.1. Heat transfer enhancement using nanofluids: The dominant modes of heat transfer enhancement using copper oxide nanoparticles and carbon nanotubes in a distilled water basefluid. Brownian motion and the associated micro-mixing is the dominant mechanism for improved heat transfer in copper oxide nanofluid. Van der Waals interaction of carbon nanotubes results in a substantially high axial heat conduction through phonon resonance across the fluid.

nels. The effects of particle size, concentration and temperature on the thermal conductivity were modelled and benchmark efficiency metrics were calculated from these heat transfer enhancements. Characterization of nanofluids was done using SEM imaging and dynamic light scattering (DLS) to analyse the stable particle size distribution in the solution. From these results, we determined the agglomeration mechanisms in nanofluids emphasizing the role of surfactants in solution stability. Finally, the effects of nanofluids on membrane fouling and surface hydrophobicity were investigated by measuring the static contact angle of water and SEM characterization of the fouled membranes.

3.2 Materials and Methods

Methods overview: Nanofluids were created by adding purchased nanoparticles along with surfactants to a base deionized water solution and mixed with stirring and sonication to disperse the nanoparticles. Dynamic light scattering (DLS) was carried out to determine the agglomerate sizes in nanofluids after different sonication durations. Thereafter, SEM images of dried nanofluid solutions and fouling tested membranes were taken to visualize the particle dispersion. The contact angle of water on fouling tested membranes was measured

to study their hydrophobicity after exposure to nanofluids. Finally, the thermal conductivity enhancements and property variations (density, specific heat and viscosity) of nanofluids were modelled to estimate the energy efficiency of MD systems using a comprehensive thermodynamic framework.

Materials and chemicals: Multi-walled carbon nanotubes (MWCNTs) with 9.5 nm average diameter, 1.5 μm average length, 250 m^2/g specific surface area and 90% purity were purchased from Nanocyl SA (Nanocyl SA, Sambreville, Belgium). Copper(II) oxide (CuO) nanoparticles with 10 nm average diameter and 99% purity, Polyvinylpyrrolidone (PVP, average MW 40,000) and Sodium dodecylbenzene sulfonate (SDBS, Purity > 99%) surfactants were obtained from Sigma-Aldrich (Sigma-Aldrich, St. Louis, MO). Unlaminated poly tetrafluoroethylene (PTFE) membrane with pore size 0.2 μm , porosity 0.8, and thickness 50 μm was purchased from Sterlitech (Sterlitech, Kent, WA).

3.2.1 Experimental methods

Preparation of Nanofluids: Copper oxide nanoparticles (for CuO-Water nanofluid) or multi-walled carbon nanotubes (for MWCNT-Water nanofluid) were added to a solution of SDBS surfactant mixed with deionized water, as shown in Figure 3.2. Magnetic stirring was carried out to break down the macroscopic lumps of SDBS and nanoparticles in the solution. In order to get nanometer scale particles, the nanofluid was subsequently sonicated (Q700 Sonicator, Qsonica, Newtown, CT) at 45% vibration amplitude and 20 kHz frequency. The SDBS surfactant helped in stabilizing the nanoparticles agglomerating in the solution and the required sonication duration varied with the desired nanofluid concentration (6 different samples were made as shown in Table 3.1).

Membrane Fouling Studies: Nanofluid solutions (copper oxide and carbon nanotubes) were circulated in a lab-scale MD module to investigate their effects on the fouling and hydrophobicity of a PTFE membrane. A 800 ml of 0.1% nanofluid solution was pumped through the feed channel for 2 hours, at a constant flow rate of 1 litre/min and a temperature of 50°C where fouling occurred. The module was flushed with deionized water before and after the test to remove surface adhered impurities and nanoparticles. Finally, the membrane

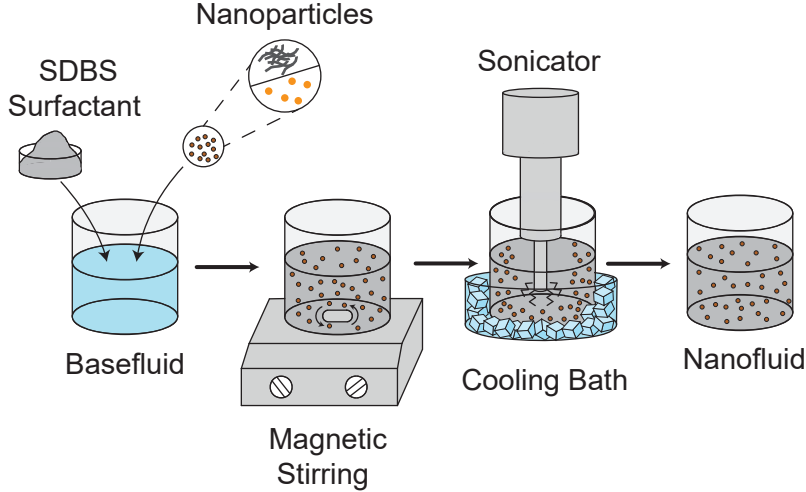


Figure 3.2. Preparation of nanofluids: Nanofluid preparation using sodium dodecylbenzenesulfonate (SDBS) surfactant and sonication. Copper oxide nanoparticles are shown as orange spheres and multi-walled carbon nanotubes are represented by gray stands (top, middle).

Table 3.1. Copper oxide (CuO) and carbon nanotube (MWCNT) nanofluids characterized for MD, with details on their concentration and sonication duration

Sample	Nanoparticle concentration	Surfactant concentration	Sonication duration	Usage
1	0.001% CuO	0.005% SDBS	180 mins	DLS studies
2	0.001% CuO	0.05% SDBS	180 mins	DLS studies
3	0.1% CuO	0.3% SDBS	80 mins	Membrane fouling
4	0.001% MWCNT	0.005% SDBS	180 mins	DLS studies
5	0.001% MWCNT	0.05% SDBS	180 mins	DLS studies
6	0.1% MWCNT	0.5% SDBS	80 mins	Membrane fouling

was cleaned under a steady stream of deionized water for 5 minutes and naturally dried for characterization.

Nanofluid and Membrane Characterization: The agglomerate sizes in nanofluids were analyzed with sonication duration using dynamic light scattering (DLS) model Malvern Zetasizer Nano ZS. 0.001% CuO-Water and MWCNT-Water nanofluids were prepared with two different SDBS surfactant concentrations (0.05 and 0.005%) and samples were taken from the solutions at specific time intervals during 3 hour sonication runs of the nanofluids. The

morphological characterizations of nanofluids and membrane fouling were obtained using field emission scanning electron microscopy (FESEM model Hitachi S-4800). Nanofluid solutions were dried on a glass plate before SEM imaging. Energy dispersive x-ray spectroscopy (EDS) was used to identify copper oxide nanoparticles in the fouling tested membrane.

3.2.2 Numerical modelling

The computational MD model was based on one-dimensional finite difference method, where properties varied along the length and were assumed to be constant along the width. Mass and energy conservation equations were solved for each discretized control volume using the built-in property evaluation functions of engineering equation solver (EES) [44]. Span-wise property variations were accounted for using thin temperature and concentration boundary layers. The nanofluids were treated as homogeneous entities with properties modified according to relations from prior literature [74]. These relations included the effects of temperature and material properties like particle size, and volume fraction on the micro-scale particle dynamics.

Nanofluid thermal conductivity relations

Nanofluids exhibit unusual enhancements in thermal conductivity at very low nanoparticle concentrations and so numerous studies have been aimed at capturing this variation both analytically and experimentally [75]–[79].

In the present analysis, an analytical study from Koo et al. [80] on the variation of thermal conductivity was adopted for CuO-Water nanofluid. Numerous reviews have supported the validity of this relation with experimental data [74], [79], [81]–[85]. The conductivity enhancements with contributions from static particle dispersion and Brownian motion of particles were derived as shown below.

$$k_{\text{eff}} = k_{\text{static}} + k_{\text{brownian}}$$

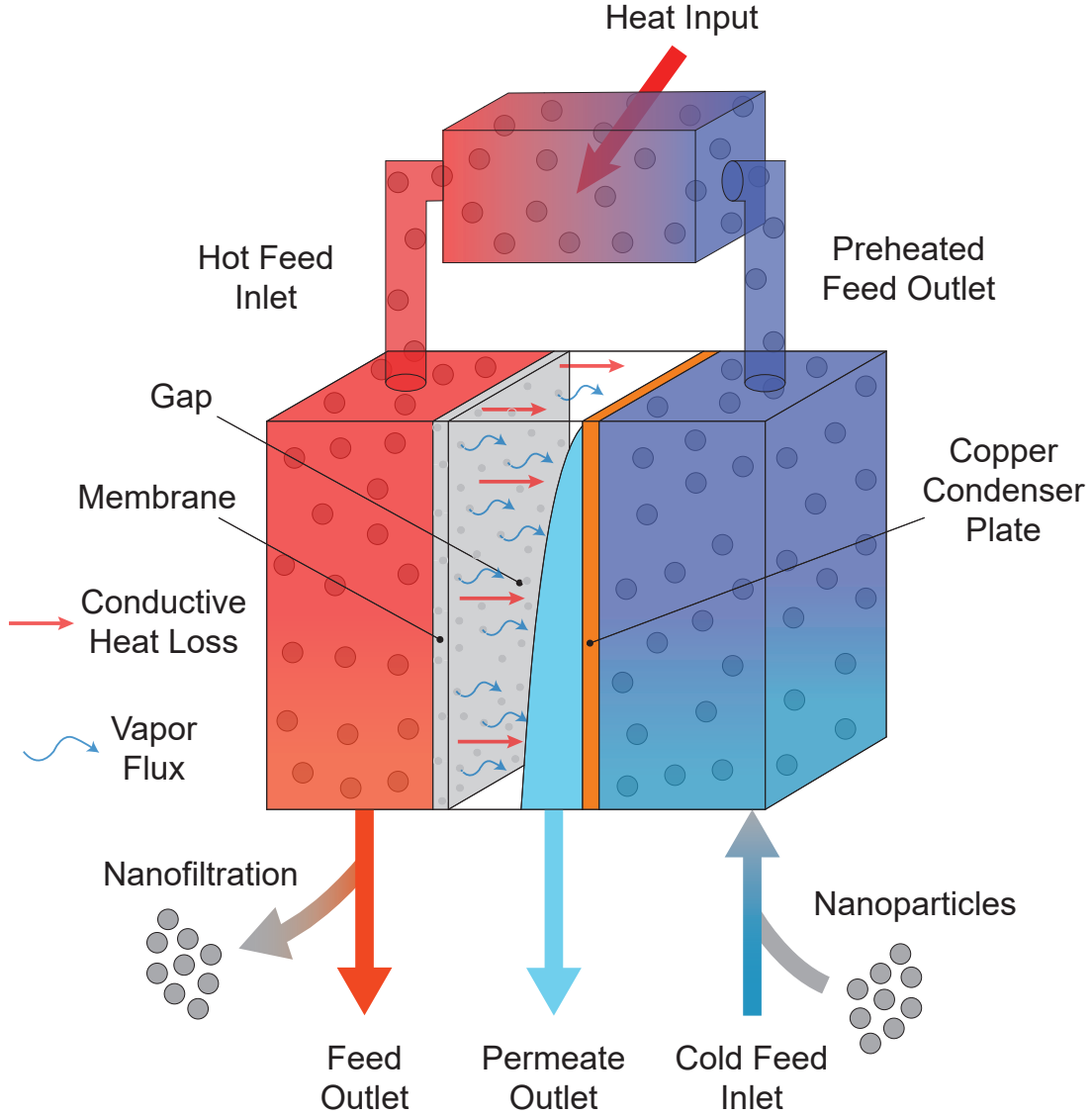


Figure 3.3. Nanofluids in membrane distillation: Membrane Distillation (MD) schematic with the addition of nanofluids. Three different configurations can be made by modifying the gap properties between the membrane and condenser plate. Air gap membrane distillation (AGMD), shown above, introduces a stagnant air medium in the gap region, permeate gap membrane distillation (PGMD) is obtained when the gap is flooded with water and finally conductive gap membrane distillation (CGMD) has conductive spacers stacked up in the gap.

The static enhancement expression used was identical to the one given by Maxwell [55],

$$\frac{k_{\text{static}}}{k_{bf}} = 1 + \frac{3\alpha_p \left(\frac{k_p}{k_{bf}} - 1 \right)}{\left(\frac{k_p}{k_{bf}} + 2 \right) - \alpha_p \left(\frac{k_p}{k_{bf}} - 1 \right)}$$

where α_p is the particle volume fraction, k_p is the thermal conductivity of nanoparticle and k_{bf} that of the base fluid. The brownian motion contribution to thermal conductivity was derived from time averaged kinetic theory [80], [86] and given as,

$$k_{\text{brownian}} = 5 * 10^4 \beta \alpha_p \rho_{bf} c_{bf} \sqrt{\frac{\kappa T}{\rho_p D}}$$

where ρ_{bf} is the density, c_{bf} is the specific heat of the base fluid, κ is the boltzmann constant, D the average diameter of particles and T the bulk temperature [80]. The term β is related to particle motion; it includes the effects of micro-mixing and is determined from experimental data. For CuO nanoparticles with concentration below 1% we have [80],

$$\beta = 0.0137 (100\alpha_p)^{-0.8229}$$

Carbon nanotubes have a fibrous structure and in order to accurately capture their interaction, a verified [87]–[89] experimental correlation from Esfe et al. [90] was used to model the MWCNT-Water nanofluid. The correlation was valid for concentrations below 1% and for temperatures between 25 - 55°C which are prevalent in most MD systems.

$$\frac{k_{nf}}{k_{bf}} = \frac{(360.69 + T)}{(405.59 - 11080\alpha_p)}$$

Nanofluid properties: density, specific heat and viscosity

Density relations for nanofluids were derived assuming a simple static distribution of nanoparticles in the basefluid, and governed by a general fractional relation [91].

$$\rho_{nf} = \rho_p \alpha_p + \rho_{bf} (1 - \alpha_p)$$

where ρ_{nf} is the density of nanofluid and ρ_{bf} is the density of basefluid. The specific heat of nanofluids followed a similar concentration based relation given as [91],

$$c_{p,nf} = \left(\frac{\rho_p}{\rho_{nf}} \right) \alpha_p c_{p,p} + \left(\frac{\rho_{bf}}{\rho_{nf}} \right) (1 - \alpha_p) c_{p,bf}$$

where $c_{p,nf}$ represents the specific heat of nanofluid, $c_{p,bf}$ is the specific heat of basefluid and $c_{p,p}$ the specific heat of nanoparticles.

The dispersion of nanoparticles in the base fluid increases the viscosity of the solution, and as a result, nanofluid viscosity correlations have been studied extensively [84], [92] to quantify the associated increased pressure drops. Here a well-validated correlation proposed by Naik and Sundar [93] was used to model the viscosity changes with particle concentration and temperature for CuO-Water nanofluids.

$$\frac{\mu_{nf}}{\mu_{bf}} = 3.444 \left(\frac{T_{\max}}{T_{\min}} \right)^{0.514} \alpha_p^{0.1829}$$

The viscosity of MWCNT-Water nanofluids was modelled using a correlation from Esfe et al. [90] given as,

$$\frac{\mu_{nf}}{\mu_{bf}} = 38.158\alpha_p - 0.0017357T + 1.1296$$

where μ_{nf} represents the viscosity of nanofluid and μ_{bf} the viscosity of basefluid.

3.3 Results and Discussion

The performance of MD systems implementing nanofluids was quantified numerically along with investigating particle size, dispersion with sonication duration, surfactant concentration and the effects of nanofluids on membrane fouling and hydrophobicity. First, the variation of thermal conductivity with particle concentration was studied at the average operating temperature of MD modules in section 3.3.1. The micro-mixing from Brownian motion significantly increased the heat transfer in copper oxide nanofluids and the Van der Waals interaction of carbon nanotubes led to substantial axial conduction through phonon resonance across the basefluid, improving its thermal conductivity. Thereafter, the energy efficiency enhancements with varying nanoparticle concentration were compared for different MD configurations outlining the relative effects of improved channel heat transfer in section 3.3.2. The optimal performance of CGMD systems was studied with particle concentration to affirm new benchmark efficiency metrics for MD in section 3.3.3.

SEM images of dried nanofluid solutions were compared before and after sonication in section 3.3.4 to check for particle agglomeration. Particle interaction directly affected the nanoscale thermal transport, with reduced Brownian motion enabled mixing in copper oxide nanofluids and increased axial conduction across carbon nanotube nanofluids. Effects of SDBS surfactant and sonication duration on the stable particle sizes in nanofluids were examined using the DLS technique in section 3.3.5. Finally, the membrane fouling and hydrophobicity were tested in section 3.3.6 using SEM imaging and static contact angle measurements after circulating nanofluids in the MD module.

3.3.1 Modelled thermal conductivity enhancements from nanofluids

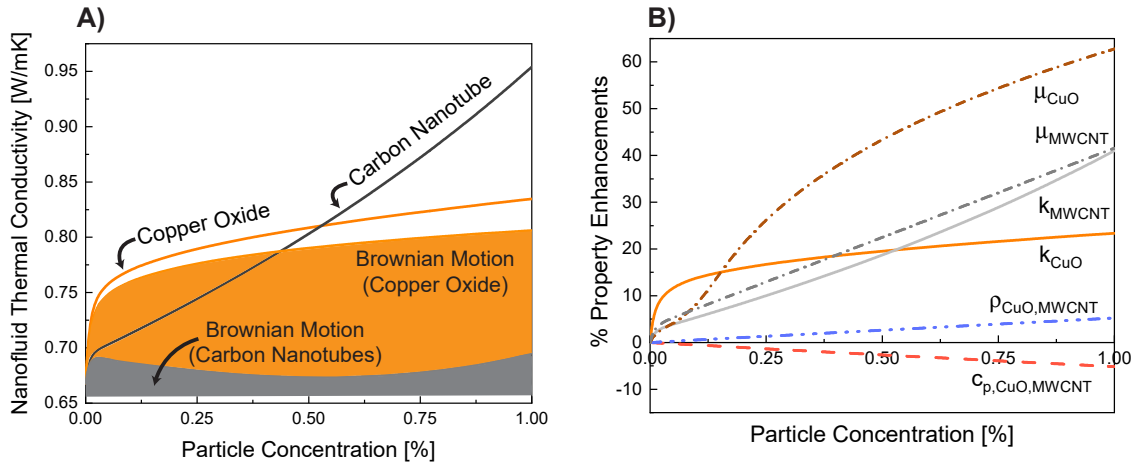


Figure 3.4. Property variations in nanofluids: **A)** Variation of thermal conductivity for CuO-Water and Carbon Nanotube (MWCNT)-Water nanofluid by particle volume fraction, where contributions to thermal conductivity from Brownian motion are shown by shaded regions. **B)** Property changes relative to seawater in the feed at various nanoparticle concentrations, including viscosity μ , density ρ , heat capacity c_p and conductivity k . Properties were evaluated at an average temperature of the MD system (55°C). Brownian motion and the interaction of particles significantly increases the nanofluid thermal conductivity compared to seawater ($0.668 [W/mK]$).

Thermal conductivity enhancements from carbon nanotubes and copper oxide nanoparticles were modelled for dilute nanofluids (below 1% concentration). Brownian motion and the related micro-mixing played a major role in increasing the thermal conductivity at very low

nanofluid concentrations as seen in Figure 3.4A. When increasing the nanoparticle concentration, agglomeration was amplified, resulting in larger particles and reducing the significance of Brownian motion. Static enhancements dominated the thermal conductivity of nanofluids at higher concentrations, eventually tapering off the conductivity curve, as seen with copper oxide nanoparticles in Figure 3.4A. The static conductive transport was particularly prominent in nanotubes where axial interactions led to long chains carrying heat across the fluid (higher slope in 3.4A) [94]. Moreover, the increased particle density for nanotubes resulted in significantly lower Brownian enhancements compared to copper oxide and showed an early transition to static thermal transport [95].

3.3.2 Relative energy efficiency of various MD configurations

The energy efficiency of thermal desalination systems is described by gained output ratio (GOR), which is defined as heat of vaporization of permeate divided by the heat input required for the MD system [1].

$$\text{GOR} = \frac{\dot{m}_{\text{per}} h_{fg}}{\dot{Q}_h}$$

where \dot{m}_{per} [kg/s] represents the permeate flux output from MD system, h_{fg} [kJ/kg] is the latent heat of vaporization and \dot{Q}_h [kW] is the thermal energy input required. Practical MD systems have GOR values ranging from 3-7 [31], [33], [96] with new configurations like vacuum-assisted air gap membrane distillation (V-AGMD) [97] peaking at 13.5.

Percentage efficiency enhancements from the nanofluids were calculated compared to using seawater in the feed channel, and plotted at varying particle concentration as shown in Figure 3.5A and 3.5B (modelling conditions given in Appendix A). The dominant heat transfer resistance of the gap region in AGMD and PGMD, limited the optimum energy benefits from using nanofluids in the feed channels. On the other hand, the CGMD configuration with high gap conductance showed remarkable increments in energy efficiency and proved to be more sensitive to the improved feed heat transfer.

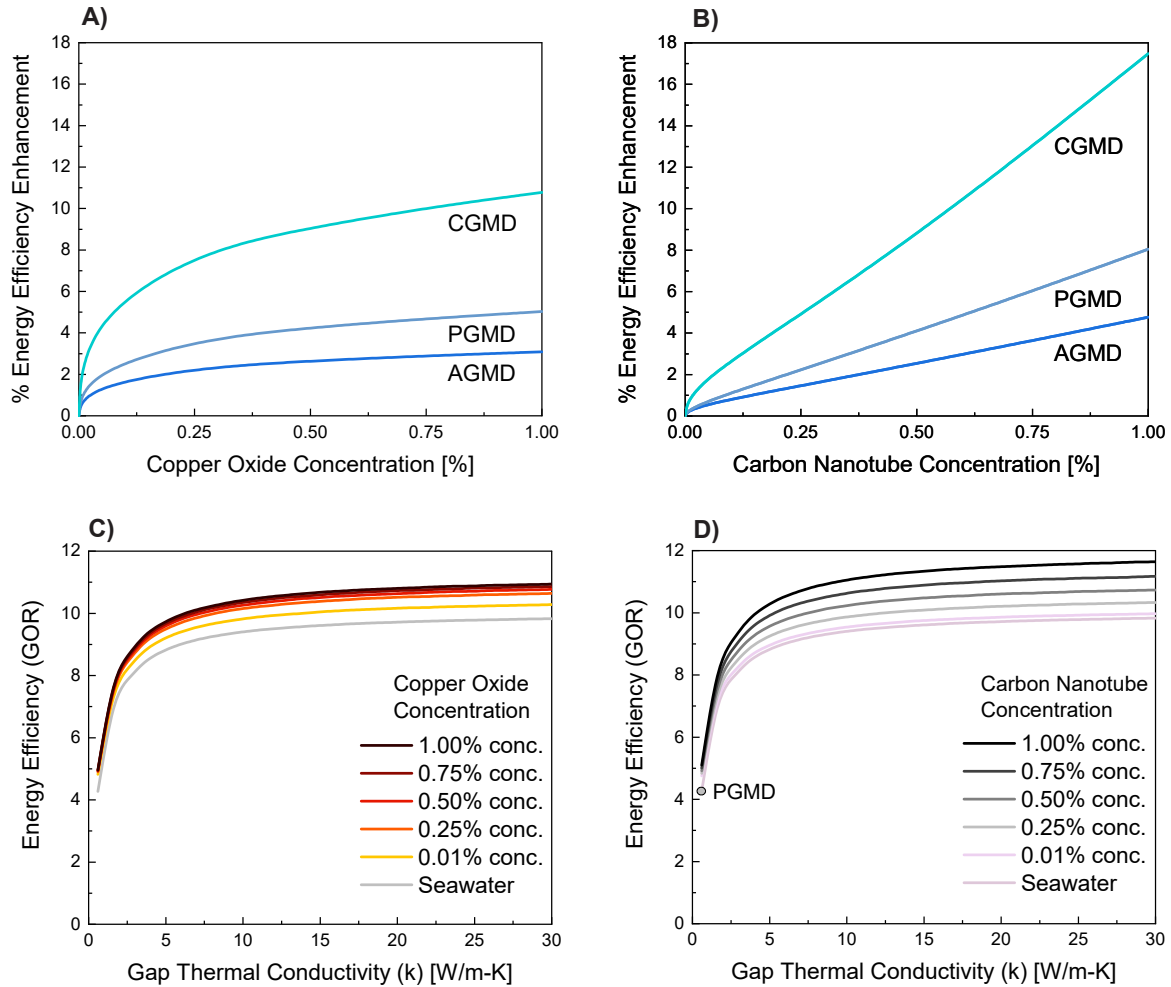


Figure 3.5. Nanofluid improvements by MD configuration: A), B) Relative enhancement of energy efficiency (GOR) with nanoparticle volume fraction for AGMD, PGMD and CGMD configurations. AGMD and PGMD configurations showed lower enhancements due to a dominant gap heat transfer resistance. **Energy efficiency (GOR) vs gap thermal conductivity:** C), D) for a CGMD configuration using nanofluids in the feed channels. Nanoparticle concentration was varied for copper oxide and carbon nanotubes along with changes to the gap thermal conductivity. A point for water flooded gap enhancement (PGMD) is also shown for comparison. The optimal performance does not change much for copper oxide nanoparticles after a concentration of roughly 0.7%, whereas carbon nanotubes show more continuous improvements. The difference is likely due to separate thermal mechanisms being dominant, as copper oxide nanofluids are highly dependant on Brownian motion, which is reduced by agglomeration at higher nanofluid concentrations.

3.3.3 Benchmark efficiency metrics for conductive gap MD systems

Modelling the energy efficiency enhancements in section 3.3.2, we observed that CGMD systems show substantial improvements using nanofluids in the feed channel. The maximum attainable energy efficiency of CGMD systems incorporating nanofluids was then evaluated at different nanoparticle concentrations (Figure 3.5C and 3.5D).

Here, we see that increasing the gap thermal conductivity in CGMD promoted higher efficiencies, but quickly had diminishing returns above $k \approx 10$ W/mK value as shown in Figure 3.5C and 3.5D. We observed that energy efficiency changes very little above a threshold gap thermal conductivity, where the thermal resistance of the gap becomes negligible [33]. This plot provided an estimation of the benchmark performance of MD resulting from improved feed channel heat transfer using nanofluids and a highly conductive gap in CGMD.

3.3.4 Particle dispersion after sonication of nanofluids

The clustering of nanoparticles significantly affects the thermal conductivity enhancements [98] and as a result, the stabilization of nanofluids using sonication and surfactants is critical. The increase in particle sizes hinders the Brownian motion at low concentrations [83], [99], [100] but results in effective liquid layering at higher concentrations [101]. This indicates that clustering reaps benefits to a certain extent, however, can also lead to sedimentation at larger characteristic sizes [102].

We investigated the effects of sonication, and surfactant addition on the stability of nanofluids and used SEM imaging to visualize the particle dispersion. The particles in a magnetically stirred nanofluid solution were compared with those in another solution sonicated for 2 hours at the same concentration. Sonication of the nanofluid reduced the micro-scale structures in the solution to nanometer sized particles for copper oxide (Figure 3.6C and 3.6D) and distinct nanometer scale strands for carbon nanotubes (Figure 3.6A and 3.6B). Moreover, the characteristic size scales observed in Figure 3.6 after sonication were larger than the nominal copper oxide particles and carbon nanotubes respectively. This indicated that particle interaction was prominent during sonication and the resulting agglomerates

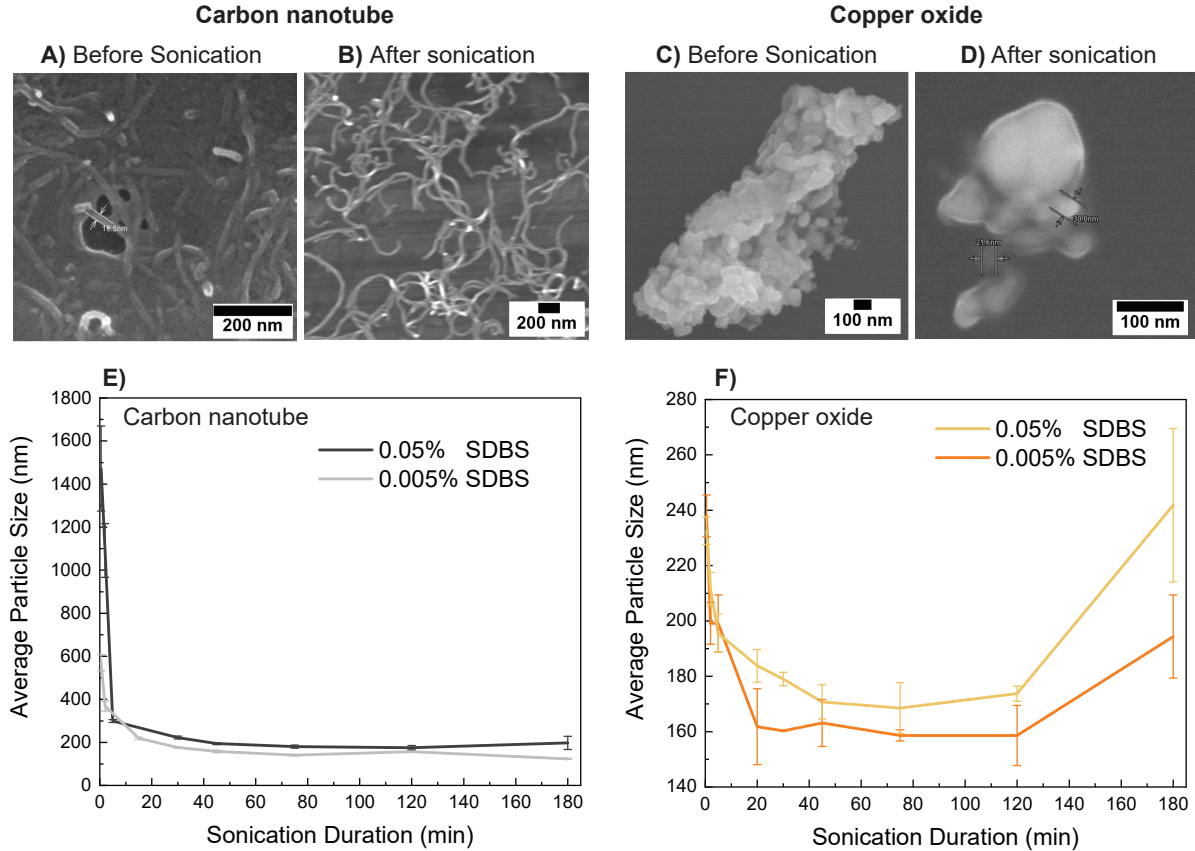


Figure 3.6. Sonication of nanofluids: Effects of sonication on the clustering of nanoparticles in 0.001% nanofluid with 0.005% SDBS solution samples dried on a glass plate. Carbon nanotubes showed massive agglomeration **A)** after magnetic stirring and were widely dispersed after 2 hours of sonication **B)**. The length of nanotube agglomerates stayed above 500 nm even after sonication due to their strong axial interaction forces. These long, surfactant stabilized nanotube strands reduce the Brownian motion but are very effective in static conduction across the fluid. Copper oxide clusters of the order of $1\ \mu\text{m}$ **C)** were broken down to characteristic size scales smaller than 200 nm **D)**, which effectively contributed to thermal conductivity enhancements from their Brownian motion. **Nanofluid particle size vs sonication, via dynamic light scattering:** Variation of average particle size of carbon nanotubes **E)** and copper oxide **F)** with sonication duration for two different concentrations of SDBS surfactant (0.05% and 0.005%). The SDBS surfactant showed reduced effectiveness above a concentration of 0.01% (yellow, 0.05% SDBS). Particle sizes increased abruptly after longer sonication durations for 0.05% SDBS concentration, due to the development of stable air bubbles in the solution which inhibited the nanoparticle cluster breakage.

were stabilized through micelle structures formed by the surrounding surfactant molecules in the solution.

3.3.5 Particle size analysis with dynamic light scattering

In order to determine the optimal surfactant concentration and sonication duration for stable solutions, we performed dynamic light scattering (DLS) studies on the nanofluids. The average particle sizes of copper oxide and carbon nanotubes decreased significantly after 20 minutes of sonication as shown in Figure 3.6E and 3.6F and then attained stability, where the interaction of nanoparticles balanced their break-up from sonication. We observed that the amount of SDBS in the solution affected the particle sizes and above a concentration of 0.01%, SDBS showed decreased effectiveness (for a 0.001% nanofluid concentration). From the results obtained in Figure 3.6E and 3.6F, we concluded that stable solutions can be made by using roughly 5 times more SDBS concentration than the required nanofluid concentration and performing at least 75 minutes of sonication. Moreover, prolonged exposure to sonication (3 hour duration in Figure 3.6E and 3.6F) resulted in the formation of bubbles in the nanofluids which inhibited the cluster breakage and led to a substantial increase in the average particle size [103]. Several studies on metal oxide [103]–[105] (alumina, zirconia and titanium dioxide) and carbon nanotube [106] nanofluids have reported this unusual observation with some cases leading to structural defects in the nanoparticles.

3.3.6 Effects of nanofluids on membrane fouling and hydrophobicity

While the surfactants help in dispersion of the nanofluids, they pose a risk to MD because they reduce the surface tension of the feed water, which can compromise the hydrophobicity of PTFE membranes [107]. As the membrane loses its hydrophobicity, mineral salts from the feed can permeate through the membrane affecting distillate quality and flux production [108], [109]. Nanofluids in the feed channel can aggravate this issue by fouling the wetted membrane, where the nanoparticles adhere to the membrane surface reducing its permeability. We investigated the effects of nanofluids with SDBS surfactant on the membrane fouling, surface hydrophobicity using SEM imaging and static contact angle measurements of water.

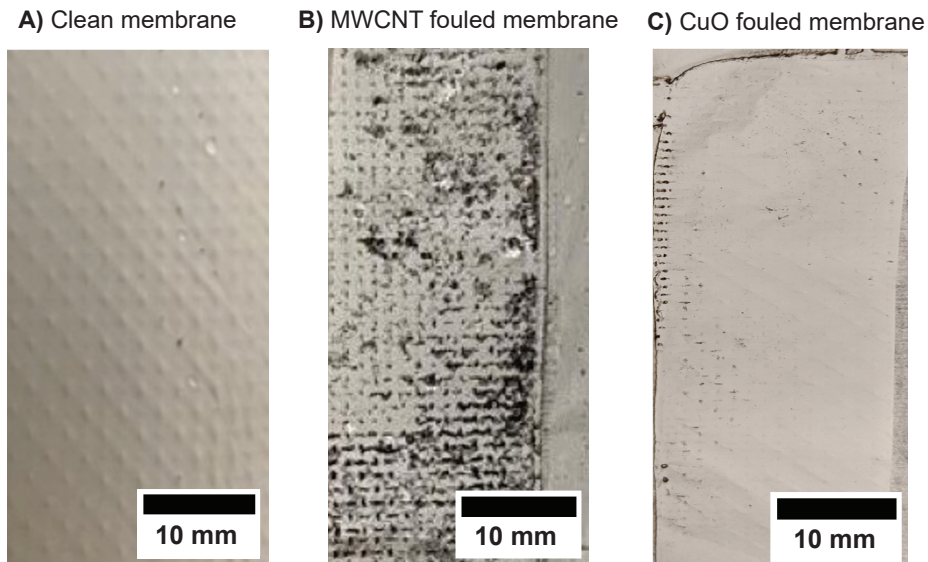


Figure 3.7. Macroscopic images of PTFE membrane after fouling tests with MWCNT and copper oxide nanofluids. Part **A)** shows a clean PTFE membrane and **B), C)** show the fouled counterparts, flushed with water for 5 minutes to remove the loosely adhered particles. Carbon nanotubes show substantial membrane fouling at the macroscale **B)** due to their higher particle density in comparison to copper oxide nanoparticles **C)**.

Macroscopic images of the PTFE membrane (Figure 3.7) after fouling tests with nanofluids, showed significant carbon nanotube deposits in comparison to copper oxide nanoparticles. MWCNT nanofluids resulted in extensive fouling of the membrane with nanotubes interacting at the microscale with PTFE fibres as seen in Figure 3.8B and 3.8E. Copper oxide nanoparticles on the other hand, showed very little fouling with some microscale agglomerate deposition on the membrane (Figure 3.8C and 3.8F). In order to quantify the decreasing membrane hydrophobicity, we measured the static contact angle of water on the fouling tested membrane samples and compared the results with that of a clean PTFE membrane.

The static contact angle of water on the membrane decreased after fouling studies with nanofluids indicating a marginal loss in membrane hydrophobicity (Figure 3.9). The contact angle measurements after using nanofluids were similar for both copper oxide and carbon nanotubes with the latter showing slightly higher variations. This was expected since the concentration of SDBS was the same in both the samples and thus would equally affect the hydrophobicity. The large variations in measurement for carbon nanotubes were the

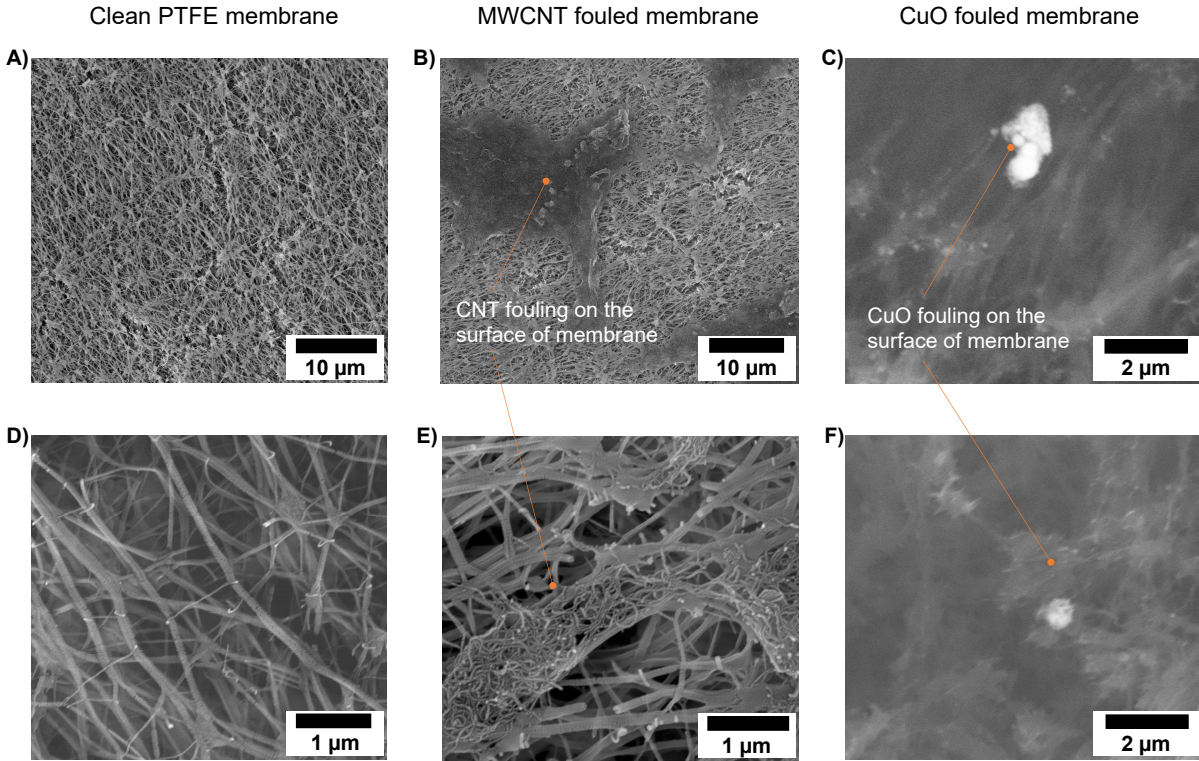


Figure 3.8. Membrane fouling from nanofluids: SEM micrographs showing the fouling of a PTFE membrane using 0.1% nanofluid solutions. Dark black spots in part **B)** show significant clustering of carbon nanotubes on the membrane surface and interactions with the membrane fibres at the microscale **E)**. SDBS surfactant reduces the surface tension of the feed, decreasing the membrane hydrophobicity and allowing nanoparticles to interact with the membrane. Nanotubes have a very high number density (number of particles per unit volume) and as a result, showed extensive membrane fouling. Negligible membrane fouling is observed using copper oxide with very few micrometer scale agglomerates **C)**, **F)** interacting with the membrane fibres. Energy dispersive x-ray spectroscopy (EDS) was used to identify the copper oxide nanoparticles in the membrane.

result of an uneven membrane surface caused by extensive fouling. We concluded that the SDBS surfactant marginally decreases the membrane hydrophobicity resulting in fouling from nanoparticles. The extent of membrane fouling can be reduced by using nanoparticles that have lower number densities (number of particles per unit volume).

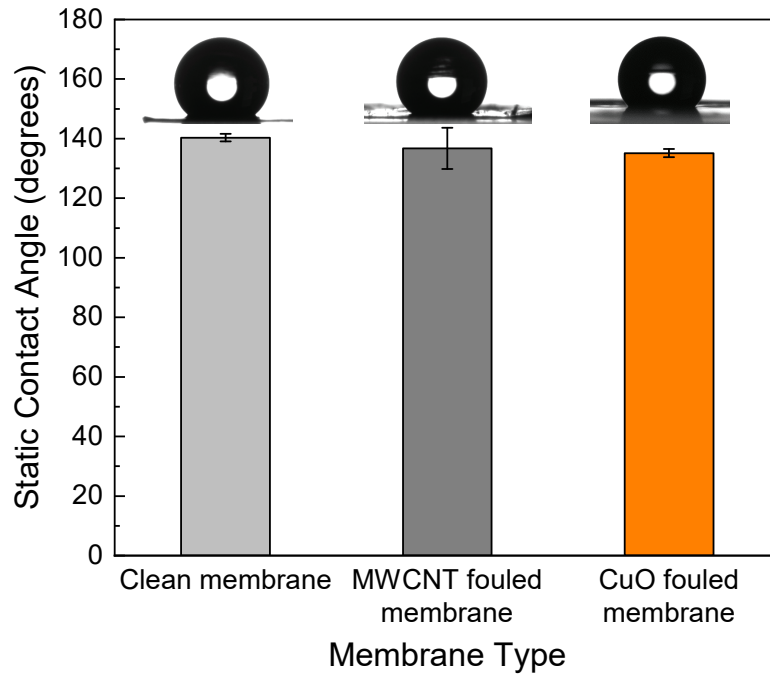


Figure 3.9. Hydrophobicity comparison of the fouled membranes: Static contact angle of water on a clean PTFE membrane and two nanofluid fouling tested PTFE membrane samples. The reduction in membrane hydrophobicity is nearly equal after using CuO-Water and MWCNT-Water nanofluids in the feed channel, since they have the same SDBS surfactant concentration. The carbon nanotube fouled membrane sample shows a relatively higher variation in measurements due to the uneven membrane surface caused by significant nanotube deposition.

4. SLIPPERY LIQUID INFUSED POROUS SURFACES (SLIPS) FOR HIGH EFFICIENCY AIR GAP MEMBRANE DISTILLATION

Disclaimer: Contents of this chapter are part of a submitted journal publication [17].

4.1 Background

4.1.1 Flooding in air gap membrane distillation

Air gap membrane distillation (AGMD) is the most versatile of all MD configurations and has the smallest sensible heat loss [22], [27], but at the same time it is limited by low permeate flux production [110]. Various studies have compared AGMD with new MD configurations like permeate gap membrane distillation (PGMD) on the basis of energy efficiency (gained output ratio i.e. GOR) and flux production rate to show the significant resistance to mass transfer offered by the air gap [5], [12], [43], [111]. As a result, there is a need to optimize the heat and mass transfer in the gap of AGMD systems for high recovery and high salinity applications [15], [112], [113].

Reducing the gap thickness in AGMD systems can improve the heat and mass transfer phenomena across the gap and result in performance enhancements [34], [114]. However, operating at gap sizes below 2 mm presents a strong possibility of flooding the air gap from the permeate being condensed inside the module [34]. Flooding is especially prominent in AGMD systems relying on film-wise condensation on metallic condenser plates for phase change and permeate removal. Moreover, the onset of flooding at a particular location decreases the mass transfer resistance across the gap and progresses into a complete flooding of the air gap making the AGMD system act like a PGMD configuration [12].

4.1.2 Novel condensation regime on SLIPS

Enhanced surfaces and surface modifications have been tested at length to promote drop-wise condensation in AGMD system (shown in Figure 4.1) and to extract all the benefits of a small air gap thickness [27], [34]. For dropwise condensation, the condensate is in the

form of discrete droplets, which are removed from the surface by gravity before they can coalesce with neighboring droplets (Figure 4.1). Moreover, the continuous removal of condensate droplets from the surface leads to replenishment of the nucleation sites for vapor to condense, with the thermal resistance significantly reduced in the absence of the additional condensate film on the condensate surface. This study marks the first comprehensive analysis of dropwise condensation on Slippery Liquid Infused Porous Surfaces (SLIPS) in membrane distillation. The performance of SLIPS in terms of energy efficiency and permeate production is examined using an in-house designed laboratory-scale AGMD system at low air gap thickness. Other parameters, such as the hot feed side temperature, and temperature difference between the hot and cold sides were varied to study their effects on the performance of SLIPS. The experimental results are then used to modify the gap transport phenomena to numerically model SLIPS inside the AGMD system and find the optimal air gap thickness at different salinities. Finally, the performance is compared with that of baseline (where plain copper surface is used) to evaluate the advantages of using SLIPS inside an AGMD system.

4.2 Modeling of SLIPS surfaces in MD

4.2.1 Overview

A one-dimensional finite difference based numerical model [12], [16], [21], [26], [27], [33], [34], [43] was developed to capture the heat transfer and thermodynamics of AGMD systems. The computational domain was discretized along the length of the module with properties assumed to be constant across the width (dimension mentioned in experimental methodology section and detailed dimensions of system can be found in Appendix B). Transport processes (heat and mass transfer) and associated property variations (salt concentration and feed temperature) across the depth were quantified using thermal and concentration boundary layers. Mass and energy conservation equations were outlined for each computational element and the resulting set of coupled equations were solved iteratively using Engineering Equation Solver (EES) [44]. The film-wise regime was modelled using a laminar flat plate condensation analysis at ambient conditions, and dropwise condensation was realized using a well-validated

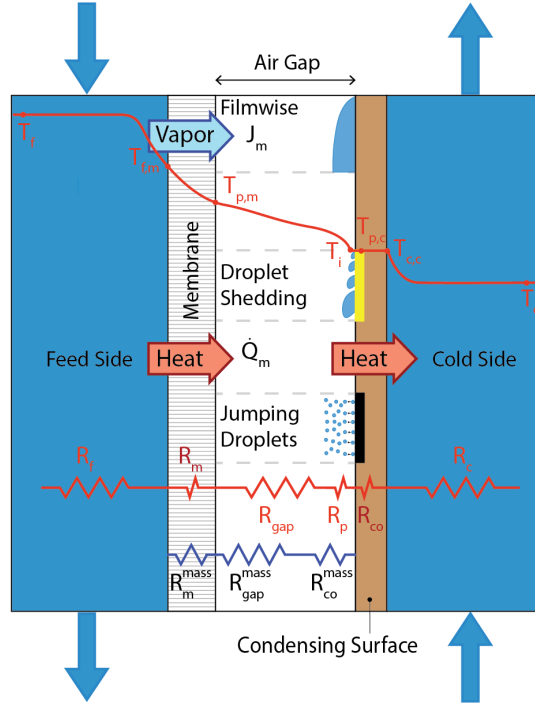


Figure 4.1. Condensation regimes in membrane distillation: Schematic of an air gap membrane distillation system showing film-wise condensation on unstructured copper surface (top), droplet shedding on SLIPS and jumping droplet condensation on superhydrophobic surfaces (below). Temperature variations across the membrane and air gap are described along with the dominant heat and mass transfer resistances in the system [17].

heat transfer correlation from Bonner [115]. The solution methodology adopted was similar to previous studies [33], [43] and accurately captured the energy efficiency of MD systems.

4.2.2 Dropwise condensation

Dropwise condensation on superhydrophobic surfaces has been considered previously to study the effects of gravity on droplet shedding and condensate removal [116], [117]. In the current work, a correlation developed by Bonner [115] was used to calculate the heat transfer coefficient associated with dropwise condensation. Several reviews and studies have considered this relation for their analysis to establish credibility [118]–[122]. A heat flux dependent

correlation was obtained by fitting experimental data available on dropwise condensation for a temperature range of 48-100°C [115] and was given as,

$$h = 2.7 \frac{k}{r_d^{1/2} r_i^{1/4} r_t^{1/4}} \left(\frac{\sin \theta}{1 - \cos \theta} \right)$$

where k represents the thermal conductivity of water, θ represents the contact angle on the condenser surface, r_d , r_i and r_t were given as,

$$r_d = \left(\frac{\sigma}{\rho g} \right)^{1/2} \quad r_i = \frac{k T_{\text{sat}}}{\rho_v h_{fg}^2} \left(\frac{\sin \theta}{1 - \cos \theta} \right) \left(\frac{\gamma + 1}{\gamma - 1} \right) \left(\frac{R_g T_{\text{sat}}}{2\pi} \right)^{1/2} \quad r_t = \frac{2\sigma T_{\text{sat}}}{\rho h_{fg} \Delta T}$$

where σ is the surface tension, ρ is the density of water, g is the acceleration due to gravity, T_{sat} is the saturation temperature of vapor at atmospheric pressure, ρ_v the density of water vapor, h_{fg} the latent heat, γ the heat capacity ratio, R_g is the specific ideal gas constant for water vapor and ΔT is the difference between the surface temperature and the saturation temperature.

The correlation involved several droplet radii to capture the physics where r_d represents the departing droplet radius, r_i represents the effective length equating conduction and interfacial resistance and r_t gives the minimum droplet radius. Some scatter was observed in the experimental data when compared with the fitted relation, but a good correspondence was maintained at average operating temperatures of MD systems (50-60°C).

4.2.3 Numerical Methodology

Experimental data for baseline tests with film-wise condensation on a copper plate was obtained and the flux, efficiency values served as foundations for comparing the performance of SLIPS enabled AGMD system and also provided a dataset for tweaking model parameters. Several model parameters were tweaked to better represent the actual transport physics. Modelling the gap transport phenomena has an intrinsic counter-flow diffusion assumption of vapor in air. However, in the experiments, mesh spacers were introduced to support the membrane which influenced the vapor and thermal transport across the gap, a tolerable

assumption [27], [34]. As shown in the lower equation D_{w-a} (diffusion coefficient) was fitted to better represent the experimental gap transport;

$$\frac{J_m}{M_w} = \frac{c_a D_{w-a}}{d_{\text{gap}} - \delta} \ln \left(1 + \frac{x_i - x_{a,m}}{x_{a,m} - 1} \right)$$

where J_m is the vapor flux, M_w is the molecular weight of water, c_a is the molar concentration of air, d_{gap} is the gap size, δ the film thickness and x is the mole fraction of vapor in the gap. Here, subscript i represents the air-water interface and the a, m subscript represents the membrane-air interface. Notably, the membrane dipped a little onto the mesh spacer with the feed flow reducing the gap size by a measured value of 0.25 mm. Equivalent gap size corrections were made to all model runs, achieving uniformity across the results. Finally, film-wise condensation would sometimes result in water drops getting trapped in the mesh spacers, and effectively increased the gap conductivity (k_{water} is roughly 0.6 compared to k_{mesh} of 0.2 W/m-K). Subsequently, the effective gap thermal conductivity was changed to take this issue into account.

Once the baseline efficiency and flux values from the numerical model were validated experimentally [17], the same parameters were used to quantify and compare the values for SLIPS enabled AGMD system. Experimental readings at four different sets of temperatures were taken with averaging from three runs for each set [17]. Numerical corrections for gap transport were carried from the baseline validation results and used in conjunction with the dropwise heat transfer correlation given in section 4.2.2.

4.3 Results and Discussions

Thermal efficiency and permeate production from AGMD systems with dropwise and film-wise condensation were modelled, and described in our analysis. Numerical algorithms formulated using the technique mentioned above are suitable for relatively large-scale systems where the assumptions of steady state and fully developed phenomena hold true. For lab-scale systems, parametric studies need to be carried out to match the modelling results with experimental observations, as done here. In section 4.3.1, the baseline flux and thermal efficiency values were matched from experiments and numerical solutions by tweaking the

gap diffusion and thermal transport coefficients. Flux values were found to be matching well but the computed thermal efficiency overshoot the experimental efficiency due to losses in the actual setup. The section 4.3.2 gives the efficiency plots for SLIPS in AGMD obtained after matching flux data from the experiments. Finally, the section 4.3.3 gives an idea of performance improvements for practical scale systems over a salinity range of 5–105 g/kg and the optimal gap sizes were obtained at each salinity.

4.3.1 Efficiency validation for baseline AGMD

The experiments and numerical model showcased improvements in thermal efficiency at higher temperatures (Figure 4.2). This metric compares energy used for evaporation with the total energy transported through the membrane; as the temperature increases, the evaporation rate increases exponentially, while conduction losses are linear. As seen in Figure 4.2, the computed efficiency values (black) obtained from matching the flux and performing parametric corrections were found to lie within the ranges of experimental (red) errors. The experimental module had inherent operating thermal losses and so efficiency was found to be consistently lower than model results.

4.3.2 Efficiency validation for SLIPS AGMD

Efficiency values from experiments and the numerical model were compared in Figure 4.3 for SLIPS enabled AGMD systems. Numerical results correlated well with experimental data, with slight deviations at low temperatures where the model slightly over-predicted efficiency. For SLIPS, droplet shedding at low flux values resulted in more water drops being essentially held in the mesh through surface tension, and so the gap conductivity increased and led to lower efficiency. In other words, gap thermal resistance was lower for SLIPS in experiments than in the SLIPS model and the experiments exhibited lower efficiency at smaller flux values. At elevated temperatures, where the flux was significantly higher (as seen in Figure 4.3), droplets had a tendency to shed through the mesh and decreased the gap conductivity a bit in accordance with the SLIPS model.

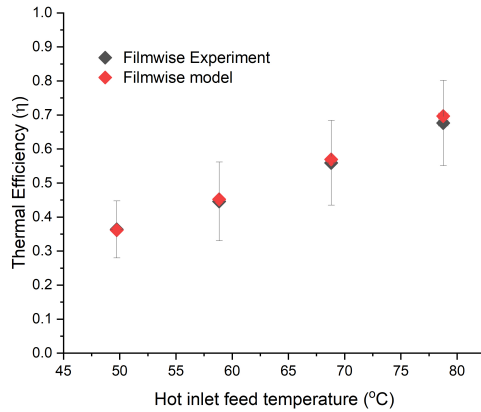


Figure 4.2. Thermal efficiency validation for film-wise condensation: Comparison of the experimental and modeling results for film-wise condensation inside a lab scale membrane distillation module. The increase in the hot feed side temperature results in a higher driving force for vapor production across the membrane. The enhancements in vapor production follow an exponential trend with temperature and outweigh the conduction losses across the membrane, thereby improving the thermal efficiency [17].

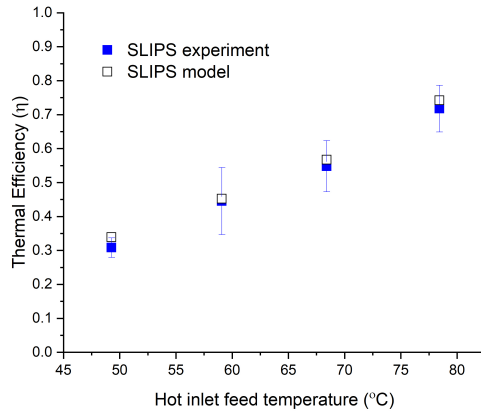


Figure 4.3. Thermal efficiency validation for SLIPS: Comparison of the experimental and modeling results for SLIPS condensation inside a lab scale membrane distillation module. Minor deviations in thermal efficiency were observed at lower feed temperatures due to the droplet entrapment in the mesh spacers at such low permeate flux values. The droplets effectively increased the thermal conductivity of the gap and resulted in higher conduction losses and compromised thermal efficiency compared to the model results [17].

4.3.3 Practical performance metrics

Lab-scale experimental tests usually involve smaller module lengths where the thermal efficiency serves well in judging performance. This metric is powerful, for practical systems as these experimental results can be extrapolated to create full scale system models that examine realizable performance enhancement from SLIPS condensation.

In AGMD, there is a key trade off caused by the air gap depth: larger depths reduce thermal conduction losses, but also increase the resistance to vapor diffusion across the gap. Therefore, for given membrane module dimensions, there exists a gap size that optimizes the energy efficiency (GOR). Here, the optimal gap thickness was determined and was used to plot Figure 4.4. Baseline frontiers for 5 and 35 g/kg feed were plotted at gap sizes that show the incipience of flooding (0.1 and 0.14 mm respectively), whereas the SLIPS frontiers at these salinities were at their optimal gap sizes. Module length was varied from 0.5 to 30 m to properly capture the GOR value peaks for the considered salinity range of 5–105 g/kg.

AGMD systems with SLIPS condensation showed higher efficiencies than film-wise systems, especially at larger module lengths. At very low salinities, the performance of both SLIPS and film-wise condensation became nearly identical, with SLIPS showing slightly higher efficiency and flux as seen in Figure 4.4. As we moved to higher salinities the distinction in efficiency of SLIPS becomes apparent and the frontiers shift downwards. Moreover, at low salinities, the optimal gap size for SLIPS was so small that film-wise condensation at these conditions resulted in flooding. As a result, film-wise condensation at 5 and 35 g/kg were modelled at the gap size before the onset flooding (0.1 and 0.14 mm respectively) whereas for other salinities gap size was identical to SLIPS.

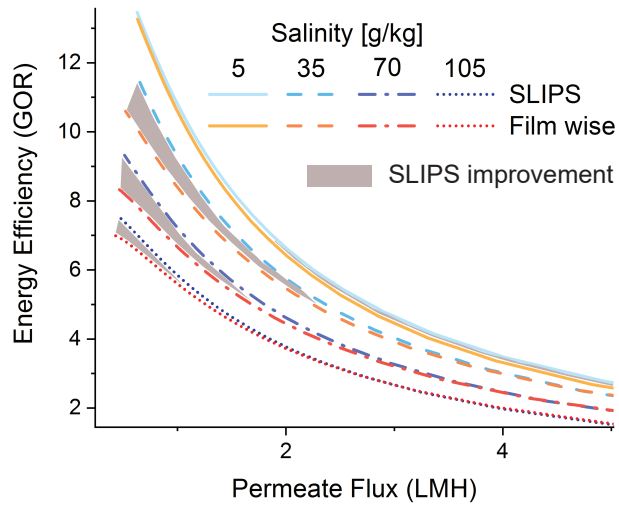


Figure 4.4. SLIPS performance improvement: Energy efficiency and permeate production with module length for SLIPS and film-wise condensation at various salinities and matching air gap sizes. Efficiency curves were plotted at the optimal gap size at each salinity for SLIPS and the enhancements were shaded for clarity. For film-wise condensation, frontiers at 5 and 35 g/kg salinities had been plotted at the gap sizes that prevent flooding (0.1 and 0.14 mm respectively) whereas for other salinities gap size was identical to SLIPS. Module length was varied from 0.5 to 30 m to properly capture the GOR value peaks for the considered salinity range of 5–105 g/kg [17].

5. POROUS CONDENSERS IN MEMBRANE DISTILLATION FOR EFFICIENT HIGH SALINITY DESALINATION

Disclaimer: Contents of this chapter are part of a submitted journal publication [18].

5.1 Heat transfer enhancements using porous condensers

Porous metallic condensers can substantially improve condensation heat transfer. Metal foams have been extensively studied in heat exchangers [123], [124] to achieve 2-3 times better heat transfer coefficients [125]–[128]. Surface modifications of these condensers have a strong effect on their wicking properties, and can be implemented to significantly reduce their thermal resistance [129], [130]. Moreover, the gravitationally driven flow regimes in these condensers make them ideal for effective passive droplet removal after their nucleation [131]. Porous condensers have been used to enhance the performance of solar stills [132], [133] and show significant promise for thermal desalination systems [134]. While not previously studied, they are particularly promising for MD systems which closely resemble heat exchangers. However, their effective integration with MD (shown in Figure 5.1) demands an overall understanding of the enhancements using lab-scale experiments and robust thermodynamic models.

In this work, we comprehensively characterized the performance of a porous condenser air gap membrane distillation system (PC-AGMD) using experiments and modelling. The results compare the energy efficiency and permeate production with leading MD configurations (AGMD, PGMD and CGMD). The performance of these MD configurations was then studied at higher salt concentrations, where PC-AGMD proved to be the most effective in desalination. The effects of permeability and thickness on the flooding of the porous condensers were modelled and the optimal wick thickness was determined to facilitate PC-AGMD module design. Finally, condensation studies were carried out on the porous condenser after being used in the membrane distillation module to visualize the droplet nucleation sites and check for flooding of the condenser.

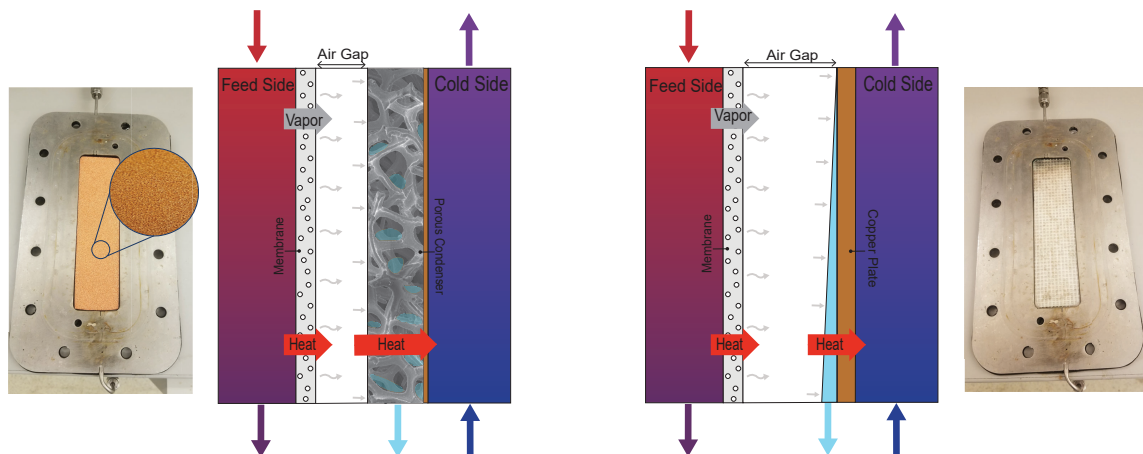


Figure 5.1. Porous condensers in membrane distillation: Experimental setup for a PC-AGMD system showing the porous copper condenser inside the membrane distillation module and an enlarged view of the porous structure. Schematic showing the heat and mass transfer across a PC-AGMD and AGMD system.

5.2 Materials and Methods

Materials and chemicals: Sodium Chloride, ACS grade, research product international, USA. Copper foam, 50 PPI, Xiamen Lith Machine Limited, and plastic mesh spacer from McMaster.

5.2.1 Experimental methods

The membrane distillation machine (Convergence Industry, BV, Netherlands) was ran with a closed-loop flow diagram. The setup was fully automatic with four PT100 temperature sensors, four pressure sensors, and two liquid flow controllers to adjust the flow. The machine was controlled with LabVIEW-based software. The PTFE unlaminated membrane filter, 0.2 micron, was supplied from Sterlitech, USA. The conductivity of the permeate was controlled using a conductivity meter (HQ40D, Hach, USA). An effective membrane area of 60 cm² (Figure 5.1) and a gap size of 3 mm was used for running flux and thermal efficiency tests of AGMD and PC-AGMD. The module was insulated with Polyurethane foam (Macmaster) to reduce the environmental heat losses. The gap size in AGMD was adjusted using a plastic

mesh and for PC-AGMD, the plastic mesh was replaced with a 3 mm copper foam. The experiment was conducted at different values of T_{feed} (50, 60, 70, 80°C) and T_{cold} (30, 40, 50, 60°C). The feed flow rate was set to 22 liters/hour and the saltwater (35 g/kg) was made using deionized water and Sodium Chloride (ACS grade, research product international, USA). Each test was ran at a constant $\Delta T = T_{\text{feed,in}} - T_{\text{cold,in}} = 20 \pm 0.44^\circ\text{C}$ and recorded two hours after stability. Five test runs of AGMD and PC-AGMD were carried out and an average of results was reported. The average pressure of the recirculation feed was set to 0.1 ± 0.05 bar.

5.2.2 Numerical methodology

The thermodynamics of MD systems have been comprehensively studied through numerical models to understand the transport phenomena [135]–[137] and their effects on energy efficiency [138] and permeate production [139]. The numerical methodology adopted in this study was based on the work from Summer et al. [43] which has been widely used and validated to characterize the performance of MD [12], [16], [17], [21], [27], [33], [34].. Here, we clarify the additional equations and modelling to model porous condensers (section 5.2.3)

A one-dimensional finite difference model was developed to capture the variation of properties along the length of the MD module. Temperature and concentration profiles along the channel width were determined using boundary layer effects. The governing equations for mass and energy conservation were solved in discretized control volumes using the property evaluation functions of engineering equation solver (EES) [44]. Mass transport through the porous condenser was modelled using the Darcy’s law for porous media flow including the effects of condenser permeability, thickness and the temperature gradient for condensation [140].

5.2.3 Heat and mass transfer through porous condensers

The analysis of condensation on porous wicks closely resembles Nusselt’s falling film theory [140]. Heat transfer across the porous condenser was governed by the local conductance

of the condenser, which in the present analysis (assuming a constant wick thickness) was given by,

$$h_c = \frac{k_{\text{wick}}}{\delta_c}$$

where h_c is the condensation heat transfer coefficient, k_{wick} is the thermal conductivity of the porous condenser with condensate and δ_c represents the thickness of the condenser. Gravitational pressure gradient drove the water vapor condensing inside the porous wick and as a result influenced the local rate of condensation. Moreover, using Darcy's law for porous media we checked for flooding of the wick when the pressure gradient became insufficient to drive the local permeate flow rate. At the incipience of flooding we defined the maximum permeate flow rate as,

$$\dot{m}_{\text{max}} = \frac{\kappa \rho \delta_c w}{\mu} \left(\frac{dp}{dz} \right)_{\text{max}} = \frac{\kappa \delta_c w \rho^2 g}{\mu}$$

where κ is the porous condenser permeability, δ_c is the thickness of condenser, w represents the width of the condenser, ρ and μ represent the density and viscosity of water respectively and g is the gravitational acceleration.

5.3 Results and Discussions

The performance of porous condensers in air gap membrane distillation was experimentally quantified, along with numerical investigations on the effects of feed salinity, condenser permeability and flooding on the transport enhancements. First, the energy efficiency and permeate production of a lab-scale porous condenser air gap membrane distillation (PC-AGMD) system were studied relative to conventional AGMD systems in section 5.3.1. The performance of these configurations was then numerically examined along with leading PGMD and CGMD configurations at commercial module length scales across varying salt concentrations in section 5.3.2. Thereafter, the optimal porous condenser thickness at different module lengths was determined in section 5.3.3 to provide guidelines for designing PC-AGMD systems. Finally, condensation imaging of the porous copper condenser was

done at atmospheric conditions to study the droplet nucleation sites and check for flooding in section 5.3.4.

5.3.1 Experimental thermal efficiency and permeate production

Porous condensers in the air gap significantly increased the permeate flux and boosted the thermal efficiency of membrane distillation, as shown in figure 5.2. The average flux improvement with porous condenser was 96.5%, with an associated thermal efficiency enhancement of 31.7%. The high porosity of the porous condenser improved the vapor condensation, by virtue of the increased surface area for condensation compared to a flat sheet condenser. Moreover, it was effective in water transport across the air gap due to the wicking properties of the condenser. The dramatic improvements in permeate flux reflected in Figure 5.2 lead to higher latent heat recovery and proportionally higher energy efficiency of the membrane distillation system.

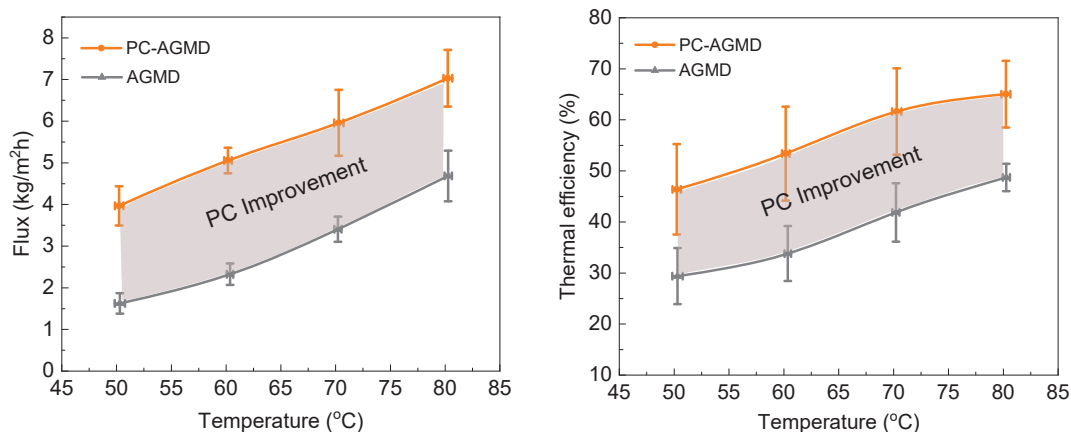


Figure 5.2. Experimental performance comparison of PC-AGMD and AGMD: Comparison of the permeate flux and thermal efficiency across different MD configurations with variations in the top temperature of the feed at seawater salinity. The average flux improvement with the porous condenser was 96.5%, and the thermal efficiency enhancement was 31.7%. Porous condensers are very effective in water transport across the air gap due to their wicking properties and result in dramatic permeate flux enhancements. Flux improvements result in increased latent heat recovery which effectively translates to higher energy efficiency.

5.3.2 Performance comparison of MD configurations

The energy efficiency (GOR) and permeate production of PC-AGMD were modelled using the conditions given in Appendix C and compared to other gap based MD configurations as shown in Figure 5.3. PC-AGMD outperformed AGMD and PGMD due to the improved conductive heat transfer across the gap and increased active surface area for vapor condensation. On the other hand, CGMD performed the best at seawater salt concentrations (especially at larger module lengths) but was significantly compromised at high salinities as observed in Figure 5.3. Overall, the PC-AGMD configuration was more efficient than its air, permeate gap counterparts and proved to be the most effective at higher salt concentrations as shown in Figure 5.3.

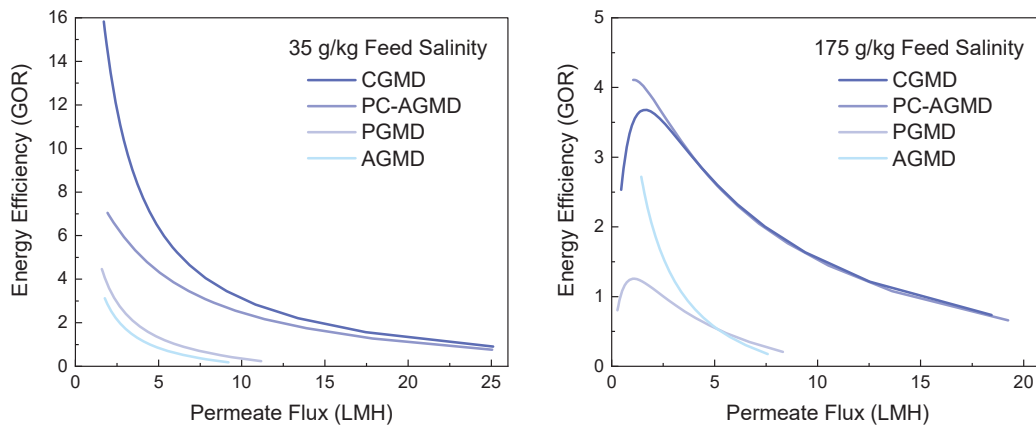


Figure 5.3. Relative performance comparison of PC-AGMD with leading MD configurations: GOR-flux frontiers across different MD configurations with variations in the module length at seawater salt concentration and high salinity (175 g/kg). PC-AGMD outperforms AGMD and PGMD due to the improved conductive heat transfer across the gap and increased active surface area for vapor condensation. CGMD performs the best at seawater salt concentrations but is significantly compromised at high salinities where PC-AGMD provides the best performance. The gap size is maintained at 3 mm across all the configurations and the rest of the modeling conditions are mentioned in the Appendix C.

5.3.3 Optimal condenser thickness for seawater desalination

The resistance to mass transfer in MD systems is a strong function of the thickness of the gap separating the membrane and the condenser. Furthermore, as the gap thickness decreases, its thermal conductance increases, which improves the overall energy efficiency of the system. We determined the optimal porous condenser thickness that results in the highest energy efficiency enhancements without flooding the condenser at increasing module lengths. Condensers with higher permeability were effective in droplet removal at smaller gap sizes and thereby achieved better energy efficiency in comparison to lower permeability wicks as seen in Figure 5.4.

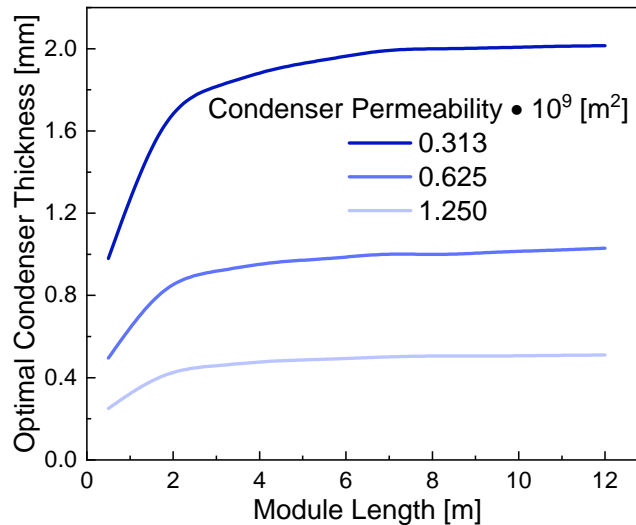


Figure 5.4. Optimized porous condenser thickness: Optimal porous condenser thickness with increasing module length at various wick permeabilities. Increasing the permeability of the condenser results in more effective droplet removal, and thus allows the operation at smaller gap sizes. Lowering the permeability promotes an early incipience of flooding in the condenser and inhibits the energy efficiency of the PC-AGMD configuration.

5.3.4 Condensation images at atmospheric conditions

Condensation inside MD systems occurs at atmospheric pressures and as a result follows the same physics as in open air, gravity driven processes. We visualized the condensation

inside the porous condenser using a high speed camera and compared images from the onset of nucleation to the formation of large droplets as shown in Figure 5.5. The pores of the metallic condenser offer ideal nucleation sites for formation of several tiny water droplets which coalesce as time progresses. However, the resulting large water droplets do not flood the pores of the condenser (as shown by red circles in Figure 5.5) and can be easily shed from the structure using gravity.

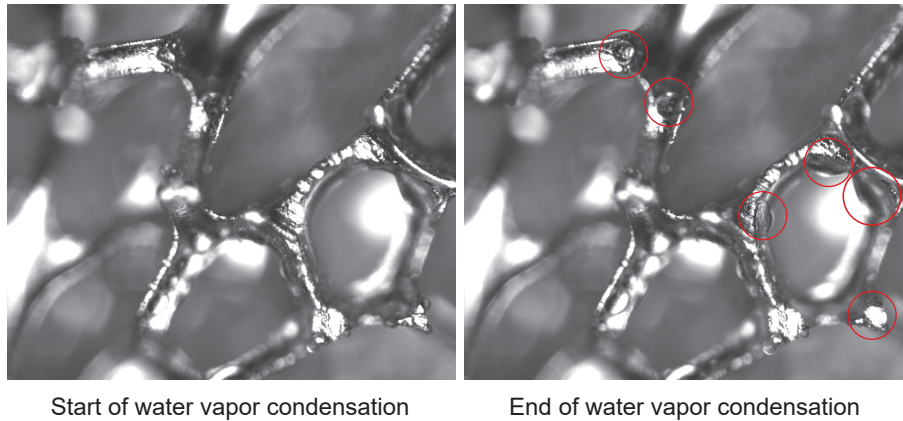


Figure 5.5. Condensation imaging of porous condensers: Open air condensation imaging of porous condensers at the beginning of droplet nucleation and after coalescence of smaller droplets to larger sizes (shown by red circles). Numerous tiny droplets are formed at the initial phase on the surface of the porous condenser indicating the availability of nucleation sites. Droplet coalescence does not flood the pores of the condenser and the large droplets are shed easily from their nucleation sites by gravity.

6. CONCLUSIONS AND FUTURE WORK

6.1 Nanofluids for energy efficient desalination

Metallic nanoparticles of characteristic size scales below an order of 100 nm can result in effective micro-mixing of the feed from their Brownian motion at low concentrations. In addition, the Van der Waal interaction of fibrous nanotubes can achieve even higher static conduction enhancements across the nanofluid. The improvements in heat transfer from these mechanisms can promote significantly higher efficiencies in membrane distillation across diverse operating conditions and system scales. However, as we demonstrated from nanofluid characterization, stable dispersions demand optimized sonication durations and surfactant concentrations. Moreover, surfactants reduced the membrane hydrophobicity and served as promoters for membrane fouling affecting the performance of MD. Dilute solutions of metallic nanofluids showed minimal membrane fouling and can be used in the channels for significant heat transfer improvements. The fouling concerns of carbon nanotubes promote their usage in heat exchangers for thermal input to MD systems, instead of directly suspending them in the channels.

6.2 Novel condensation surfaces enhance high salinity desalination

The performance of air gap membrane distillation (AGMD) using SLIPS surface for vapor condensation was comprehensively studied and compared to film-wise condensation through experiments and numerical analysis. Condensation images on SLIPS surfaces showcased tiny droplet nucleation sites marking their potential to operate at small air gap thickness without flooding. The flux production is higher for SLIPS at all temperatures compared to film-wise condensation on a copper plate showing that the improved condensation regime help in faster droplet removal from the surface and increases the available nucleation sites. The modelled optimal air gap thickness for the highest efficiency at different salinities for SLIPS and filwise condensation are markedly different and the baseline copper surface floods at an air gap thickness equal to the optimal air gap thickness for SLIPS.

Gravitationally driven wicking properties and the increased droplet nucleation sites in porous condensers significantly enhance the mass transport in gap based membrane distillation systems. Additionally, the high thermal conductivity of the metallic structure results in effective latent heat removal and superior heat recovery in MD. The average flux improvement with porous condenser was 96.5%, with an associated thermal efficiency enhancement of 31.7%. Delayed incipience of flooding in our PC-AGMD configuration is especially beneficial for high salinity desalination where equivalent PGMD and CGMD systems show poor performance. However, porous condensers are only compatible with flat plate module designs and thus are limited in their applicability to commercial spiral wound module designs.

6.3 Future work

The success of the Brownian motion and axial conduction enhancement mechanisms suggests that other magnetic nanoparticles and hybrid nanofluids can be used in MD owing to their controllability and ease of separation. In conjunction, special membrane modifications that help in retaining their hydrophobicity at higher nanofluid concentrations can further push the performance frontiers in MD.

Our experimental studies showed that SLIPS can achieve higher efficiencies by operating at lower gap sizes compared to baseline copper surface and further tests need to be done to evaluate the impact of leakage of the lubricant into the condensate over time by performing permeate quality tests. Moreover, experimental investigations into the flooding of the porous condensers are needed to validate the expected performance enhancements and provide a comprehensive characterization of the condensation regime.

Finally, configurations like vacuum membrane distillation (VMD) [141]–[145] and vacuum air gap membrane distillation (VAGMD) [97], [146], [147], supplement the thermal driving force in MD using an applied pressure gradient and significantly enhance the permeate production. However, maintaining extremely low gap pressures is challenging and as a result these diffusion-less regimes aren't frequently accessed in MD. As a result, understanding is still lacking on the further jump in flux at very low air pressures, where diffusion is no longer significant. Accurately capturing the rapid heat and mass transfer physics in such

multiphase systems at low pressures has the potential to lead the design of high recovery thermal desalination.

REFERENCES

- [1] H. F. J. David M. Warsinger Sina Nejati, “Energy efficiency metrics in membrane distillation,” in *Advances in Water Desalination Technologies*, Y. Cohen, Ed., World Scientific Publishing Company.
- [2] D. M. Warsinger, H. Fattahijuybari, H. B. Parmar, M. Rezai, S. Nejati, and L. M. Camacho, “Unifying efficiency metrics for solar evaporation and thermal desalination,” *Energy and Environmental Science*, 2021.
- [3] M. Elimelech and W. A. Phillip, “The future of seawater desalination: Energy, technology, and the environment,” *science*, vol. 333, no. 6043, pp. 712–717, 2011.
- [4] M. S. Mauter, I. Zucker, F. Perreault, J. R. Werber, J.-H. Kim, and M. Elimelech, “The role of nanotechnology in tackling global water challenges,” *Nature Sustainability*, vol. 1, no. 4, pp. 166–175, 2018.
- [5] A. Deshmukh, C. Boo, V. Karanikola, S. Lin, A. P. Straub, T. Tong, D. M. Warsinger, and M. Elimelech, “Membrane distillation at the water-energy nexus: Limits, opportunities, and challenges,” *Energy & Environmental Science*, vol. 11, no. 5, pp. 1177–1196, 2018.
- [6] P. Goh, T. Matsuura, A. Ismail, and N. Hilal, “Recent trends in membranes and membrane processes for desalination,” *Desalination*, vol. 391, pp. 43–60, 2016.
- [7] S. Al-Obaidani, E. Curcio, F. Macedonio, G. Di Profio, H. Al-Hinai, and E. Drioli, “Potential of membrane distillation in seawater desalination: Thermal efficiency, sensitivity study and cost estimation,” *Journal of Membrane Science*, vol. 323, no. 1, pp. 85–98, 2008.
- [8] V. Karanikola, S. E. Moore, A. Deshmukh, R. G. Arnold, M. Elimelech, and A. E. Sáez, “Economic performance of membrane distillation configurations in optimal solar thermal desalination systems,” *Desalination*, vol. 472, p. 114 164, 2019.
- [9] M. Hardikar, I. Marquez, and A. Achilli, “Emerging investigator series: Membrane distillation and high salinity: Analysis and implications,” *Environmental Science: Water Research & Technology*, vol. 6, no. 6, pp. 1538–1552, 2020.
- [10] J. Li, Y. Guan, F. Cheng, and Y. Liu, “Treatment of high salinity brines by direct contact membrane distillation: Effect of membrane characteristics and salinity,” *Chemosphere*, vol. 140, pp. 143–149, 2015.

- [11] M. E. Leitch, C. Li, O. Ikkala, M. S. Mauter, and G. V. Lowry, “Bacterial nanocellulose aerogel membranes: Novel high-porosity materials for membrane distillation,” *Environmental Science & Technology Letters*, vol. 3, no. 3, pp. 85–91, 2016.
- [12] J. Swaminathan, H. W. Chung, D. M. Warsinger, *et al.*, “Energy efficiency of membrane distillation up to high salinity: Evaluating critical system size and optimal membrane thickness,” *Applied Energy*, vol. 211, pp. 715–734, 2018.
- [13] M. Khayet, “Solar desalination by membrane distillation: Dispersion in energy consumption analysis and water production costs (a review),” *Desalination*, vol. 308, pp. 89–101, 2013.
- [14] A. G. Fane, R. Schofield, and C. J. D. Fell, “The efficient use of energy in membrane distillation,” *Desalination*, vol. 64, pp. 231–243, 1987.
- [15] A. M. Alklaibi and N. Lior, “Transport analysis of air-gap membrane distillation,” *Journal of membrane science*, vol. 255, no. 1-2, pp. 239–253, 2005.
- [16] H. B. Parmar, H. Fattahijuybari, Y. S. Yogi, S. Nejati, R. Jacob, P. Menon, and D. M. Warsinger, “Nanofluids improve energy efficiency of membrane distillation,” *In review: Nano Energy*, 2021.
- [17] Y. S. Yogi, H. B. Parmar, H. Fattahijuybari, *et al.*, “Slippery liquid infused porous condenser surfaces (slips) for high efficiency air gap membrane distillation,” *Submitted to ACS applied materials and interfaces*, 2021.
- [18] H. B. Parmar, H. Fattahijuybari, A. Alshubbar, K. L. Young, and D. M. Warsinger, “Porous condensers for effective mass transport in membrane distillation,” *Submitted to Desalination*, 2021.
- [19] S. Lin, N. Y. Yip, and M. Elimelech, “Direct contact membrane distillation with heat recovery: Thermodynamic insights from module scale modeling,” *Journal of membrane science*, vol. 453, pp. 498–515, 2014.
- [20] E. Curcio and E. Drioli, “Membrane distillation and related operations—a review,” *Separation and Purification Reviews*, vol. 34, no. 1, pp. 35–86, 2005.
- [21] J. Swaminathan, H. W. Chung, D. M. Warsinger, *et al.*, “Membrane distillation model based on heat exchanger theory and configuration comparison,” *Applied Energy*, vol. 184, pp. 491–505, 2016.
- [22] K. W. Lawson and D. R. Lloyd, “Membrane distillation,” *Journal of membrane Science*, vol. 124, no. 1, pp. 1–25, 1997.

- [23] A. Alkudhiri, N. Darwish, and N. Hilal, “Membrane distillation: A comprehensive review,” *Desalination*, vol. 287, pp. 2–18, 2012.
- [24] P. Wang and T.-S. Chung, “Recent advances in membrane distillation processes: Membrane development, configuration design and application exploring,” *Journal of membrane science*, vol. 474, pp. 39–56, 2015.
- [25] M. Khayet and T. Matsuura, “Membrane distillation: Principles and applications,” 2011.
- [26] D. E. M. Warsinger, J. Swaminathan, and J. H. Lienhard, “Effect of module inclination angle on air gap membrane distillation,” 2014.
- [27] D. E. Warsinger, J. Swaminathan, L. A. Maswadeh, *et al.*, “Superhydrophobic condenser surfaces for air gap membrane distillation,” *Journal of Membrane Science*, vol. 492, pp. 578–587, 2015.
- [28] L. M. Camacho, L. Dumée, J. Zhang, J.-d. Li, M. Duke, J. Gomez, S. Gray, *et al.*, “Advances in membrane distillation for water desalination and purification applications,” *Water*, vol. 5, no. 1, pp. 94–196, 2013.
- [29] D. Winter, J. Koschikowski, and M. Wieghaus, “Desalination using membrane distillation: Experimental studies on full scale spiral wound modules,” *Journal of Membrane Science*, vol. 375, no. 1-2, pp. 104–112, 2011.
- [30] A. Cipollina, M. Di Sparti, A. Tamburini, and G. Micale, “Development of a membrane distillation module for solar energy seawater desalination,” *Chemical engineering research and design*, vol. 90, no. 12, pp. 2101–2121, 2012.
- [31] G. Zaragoza, A. Ruiz-Aguirre, and E. Guillén-Burrieza, “Efficiency in the use of solar thermal energy of small membrane desalination systems for decentralized water production,” *Applied Energy*, vol. 130, pp. 491–499, 2014.
- [32] Z. Ma, T. D. Davis, J. R. Irish, and G. D. Winch, *Membrane distillation system and method*, US patent app., 12/694,757 [January 27 2010].
- [33] J. Swaminathan, H. W. Chung, D. M. Warsinger, F. A. AlMarzooqi, H. A. Arafat, *et al.*, “Energy efficiency of permeate gap and novel conductive gap membrane distillation,” *Journal of Membrane Science*, vol. 502, pp. 171–178, 2016.
- [34] D. M. Warsinger, J. Swaminathan, L. L. Morales, *et al.*, “Comprehensive condensation flow regimes in air gap membrane distillation: Visualization and energy efficiency,” *Journal of membrane science*, vol. 555, pp. 517–528, 2018.

- [35] X. Yang, H. Yu, R. Wang, and A. G. Fane, “Analysis of the effect of turbulence promoters in hollow fiber membrane distillation modules by computational fluid dynamic (cfd) simulations,” *Journal of membrane science*, vol. 415, pp. 758–769, 2012.
- [36] J. A. Kharraz, M. Bilad, and H. A. Arafat, “Flux stabilization in membrane distillation desalination of seawater and brine using corrugated pvdf membranes,” *Journal of Membrane Science*, vol. 495, pp. 404–414, 2015.
- [37] L. Francis, N. Ghaffour, A. A. Alsaadi, and G. L. Amy, “Material gap membrane distillation: A new design for water vapor flux enhancement,” *Journal of membrane science*, vol. 448, pp. 240–247, 2013.
- [38] A. Alkudhiri, N. Darwish, and N. Hilal, “Treatment of high salinity solutions: Application of air gap membrane distillation,” *Desalination*, vol. 287, pp. 55–60, 2012.
- [39] S. P. Agashichev and A. Sivakov, “Modeling and calculation of temperature-concentration polarisation in the membrane distillation process (md),” *Desalination*, vol. 93, no. 1-3, pp. 245–258, 1993.
- [40] L. Martínez-Díez and M. I. Vazquez-Gonzalez, “Temperature and concentration polarization in membrane distillation of aqueous salt solutions,” *Journal of membrane science*, vol. 156, no. 2, pp. 265–273, 1999.
- [41] H. Chang, J.-S. Liau, C.-D. Ho, and W.-H. Wang, “Simulation of membrane distillation modules for desalination by developing user’s model on aspen plus platform,” *Desalination*, vol. 249, no. 1, pp. 380–387, 2009.
- [42] G. Zuo, R. Wang, R. Field, and A. G. Fane, “Energy efficiency evaluation and economic analyses of direct contact membrane distillation system using aspen plus,” *Desalination*, vol. 283, pp. 237–244, 2011.
- [43] E. K. Summers, H. A. Arafat, *et al.*, “Energy efficiency comparison of single-stage membrane distillation (md) desalination cycles in different configurations,” *Desalination*, vol. 290, pp. 54–66, 2012.
- [44] S.A.Klein, *Engineering equation solver version 10*.
- [45] A. Mills, *Heat and mass transfer*, Irwin, Boston, MA, 1992.
- [46] Y. Xuan and Q. Li, “Heat transfer enhancement of nanofluids,” *International Journal of heat and fluid flow*, vol. 21, no. 1, pp. 58–64, 2000.

- [47] D. Wen and Y. Ding, “Experimental investigation into convective heat transfer of nanofluids at the entrance region under laminar flow conditions,” *International journal of heat and mass transfer*, vol. 47, no. 24, pp. 5181–5188, 2004.
- [48] A. Ghozatloo, A. Rashidi, and M. Shariaty-Niassar, “Convective heat transfer enhancement of graphene nanofluids in shell and tube heat exchanger,” *Experimental Thermal and Fluid Science*, vol. 53, pp. 136–141, 2014.
- [49] V. Trisaksri and S. Wongwises, “Critical review of heat transfer characteristics of nanofluids,” *Renewable and sustainable energy reviews*, vol. 11, no. 3, pp. 512–523, 2007.
- [50] J. Eastman, “Novel thermal properties of nanostructured materials.,” Argonne National Lab., IL (US), Tech. Rep., 1999.
- [51] R. S. Vajjha and D. K. Das, “A review and analysis on influence of temperature and concentration of nanofluids on thermophysical properties, heat transfer and pumping power,” *International journal of heat and mass transfer*, vol. 55, no. 15-16, pp. 4063–4078, 2012.
- [52] A. M. Hussein, K. Sharma, R. Bakar, and K. Kadirgama, “A review of forced convection heat transfer enhancement and hydrodynamic characteristics of a nanofluid,” *Renewable and Sustainable Energy Reviews*, vol. 29, pp. 734–743, 2014.
- [53] M. Chandrasekar, S. Suresh, and T. Senthilkumar, “Mechanisms proposed through experimental investigations on thermophysical properties and forced convective heat transfer characteristics of various nanofluids—a review,” *Renewable and Sustainable Energy Reviews*, vol. 16, no. 6, pp. 3917–3938, 2012.
- [54] R. L. Webb, “Principles of enhanced heat transfer,” *John Wiley & Sons., NY*, 1993.
- [55] J. Maxwell, *A treatise on electricity and magnetism. 2nd edn. niven*, 1881.
- [56] R. L. Hamilton and O. Crosser, “Thermal conductivity of heterogeneous two-component systems,” *Industrial & Engineering chemistry fundamentals*, vol. 1, no. 3, pp. 187–191, 1962.
- [57] Y. Xuan and Q. Li, “Heat transfer enhancement of nanofluids,” *International Journal of heat and fluid flow*, vol. 21, no. 1, pp. 58–64, 2000.
- [58] Y. Yang, Z. G. Zhang, E. A. Grulke, W. B. Anderson, and G. Wu, “Heat transfer properties of nanoparticle-in-fluid dispersions (nanofluids) in laminar flow,” *International journal of heat and mass transfer*, vol. 48, no. 6, pp. 1107–1116, 2005.

- [59] U. Rea, T. McKrell, L.-w. Hu, and J. Buongiorno, “Laminar convective heat transfer and viscous pressure loss of alumina–water and zirconia–water nanofluids,” *International Journal of Heat and Mass Transfer*, vol. 52, no. 7-8, pp. 2042–2048, 2009.
- [60] K. S. Hwang, S. P. Jang, and S. U. Choi, “Flow and convective heat transfer characteristics of water-based Al_2O_3 nanofluids in fully developed laminar flow regime,” *International journal of heat and mass transfer*, vol. 52, no. 1-2, pp. 193–199, 2009.
- [61] B. C. Pak and Y. I. Cho, “Hydrodynamic and heat transfer study of dispersed fluids with submicron metallic oxide particles,” *Experimental Heat Transfer an International Journal*, vol. 11, no. 2, pp. 151–170, 1998.
- [62] A. Sajadi and M. Kazemi, “Investigation of turbulent convective heat transfer and pressure drop of TiO_2 /water nanofluid in circular tube,” *International Communications in Heat and Mass Transfer*, vol. 38, no. 10, pp. 1474–1478, 2011.
- [63] P. Keblinski, S. Phillpot, S. Choi, and J. Eastman, “Mechanisms of heat flow in suspensions of nano-sized particles (nanofluids),” *International journal of heat and mass transfer*, vol. 45, no. 4, pp. 855–863, 2002.
- [64] Y. Xuan, Q. Li, and W. Hu, “Aggregation structure and thermal conductivity of nanofluids,” *AIChE Journal*, vol. 49, no. 4, pp. 1038–1043, 2003.
- [65] D. Lee, “Thermophysical properties of interfacial layer in nanofluids,” *Langmuir*, vol. 23, no. 11, pp. 6011–6018, 2007.
- [66] A. K. Hussein, “Applications of nanotechnology to improve the performance of solar collectors—recent advances and overview,” *Renewable and Sustainable Energy Reviews*, vol. 62, pp. 767–792, 2016.
- [67] T. Arunkumar, K. Raj, D. Denkenberger, and R. Velraj, “Heat carrier nanofluids in solar still—a review,” *Desalin. Water Treat.*, vol. 130, pp. 1–16, 2018.
- [68] P. Goh, A. Ismail, and T. Matsuura, “Perspective and roadmap of energy-efficient desalination integrated with nanomaterials,” *Separation & Purification Reviews*, vol. 47, no. 2, pp. 124–141, 2018.
- [69] S. Sharshir, G. Peng, L. Wu, N. Yang, F. Essa, A. Elsheikh, S. I. Mohamed, and A. Kabeel, “Enhancing the solar still performance using nanofluids and glass cover cooling: Experimental study,” *Applied Thermal Engineering*, vol. 113, pp. 684–693, 2017.

- [70] W. Chen, C. Zou, X. Li, and L. Li, “Experimental investigation of sic nanofluids for solar distillation system: Stability, optical properties and thermal conductivity with saline water-based fluid,” *International Journal of Heat and Mass Transfer*, vol. 107, pp. 264–270, 2017.
- [71] A. Kabeel and E. M. El-Said, “Applicability of flashing desalination technique for small scale needs using a novel integrated system coupled with nanofluid-based solar collector,” *Desalination*, vol. 333, no. 1, pp. 10–22, 2014.
- [72] M. Bhadra, S. Roy, and S. Mitra, “Nanodiamond immobilized membranes for enhanced desalination via membrane distillation,” *Desalination*, vol. 341, pp. 115–119, 2014.
- [73] H.-C. Chen, Y.-R. Chen, K.-H. Yang, C.-P. Yang, K.-L. Tung, M.-J. Lee, J.-H. Shih, and Y.-C. Liu, “Effective reduction of water molecules’ interaction for efficient water evaporation in desalination,” *Desalination*, vol. 436, pp. 91–97, 2018.
- [74] K. Khanafer and K. Vafai, “A critical synthesis of thermophysical characteristics of nanofluids,” *International journal of heat and mass transfer*, vol. 54, no. 19-20, pp. 4410–4428, 2011.
- [75] I. Nkurikiyimfura, Y. Wang, and Z. Pan, “Heat transfer enhancement by magnetic nanofluids—a review,” *Renewable and Sustainable Energy Reviews*, vol. 21, pp. 548–561, 2013.
- [76] R. Prasher, P. Bhattacharya, and P. E. Phelan, “Thermal conductivity of nanoscale colloidal solutions (nanofluids),” *Physical review letters*, vol. 94, no. 2, p. 025 901, 2005.
- [77] Y. Li, S. Tung, E. Schneider, S. Xi, *et al.*, “A review on development of nanofluid preparation and characterization,” *Powder technology*, vol. 196, no. 2, pp. 89–101, 2009.
- [78] P. K. Das, “A review based on the effect and mechanism of thermal conductivity of normal nanofluids and hybrid nanofluids,” *Journal of Molecular Liquids*, vol. 240, pp. 420–446, 2017.
- [79] X.-Q. Wang and A. S. Mujumdar, “Heat transfer characteristics of nanofluids: A review,” *International journal of thermal sciences*, vol. 46, no. 1, pp. 1–19, 2007.
- [80] J. Koo and C. Kleinstreuer, “A new thermal conductivity model for nanofluids,” *Journal of Nanoparticle research*, vol. 6, no. 6, pp. 577–588, 2004.
- [81] W. Yu, D. M. France, J. L. Routbort, and S. U. Choi, “Review and comparison of nanofluid thermal conductivity and heat transfer enhancements,” *Heat transfer engineering*, vol. 29, no. 5, pp. 432–460, 2008.

- [82] O. Mahian, A. Kianifar, S. A. Kalogirou, I. Pop, and S. Wongwises, “A review of the applications of nanofluids in solar energy,” *International Journal of Heat and Mass Transfer*, vol. 57, no. 2, pp. 582–594, 2013.
- [83] H. A. Mintsa, G. Roy, C. T. Nguyen, and D. Doucet, “New temperature dependent thermal conductivity data for water-based nanofluids,” *International journal of thermal sciences*, vol. 48, no. 2, pp. 363–371, 2009.
- [84] C. Nguyen, F. Desgranges, G. Roy, N. Galanis, T. Maré, e. Boucher, and H. A. Mintsa, “Temperature and particle-size dependent viscosity data for water-based nanofluids—hysteresis phenomenon,” *International journal of heat and fluid flow*, vol. 28, no. 6, pp. 1492–1506, 2007.
- [85] M. Corcione, “Empirical correlating equations for predicting the effective thermal conductivity and dynamic viscosity of nanofluids,” *Energy conversion and management*, vol. 52, no. 1, pp. 789–793, 2011.
- [86] S. Chapman, T. G. Cowling, and D. Burnett, *The mathematical theory of non-uniform gases: an account of the kinetic theory of viscosity, thermal conduction and diffusion in gases*. Cambridge university press, 1990.
- [87] O. Mahian, L. Kolsi, M. Amani, P. Estellé, G. Ahmadi, C. Kleinstreuer, J. S. Marshall, M. Siavashi, R. A. Taylor, H. Niazmand, *et al.*, “Recent advances in modeling and simulation of nanofluid flows—part i: Fundamentals and theory,” *Physics reports*, vol. 790, pp. 1–48, 2019.
- [88] M. Afrand, K. N. Najafabadi, and M. Akbari, “Effects of temperature and solid volume fraction on viscosity of SiO_2 -mWCNTs/sae40 hybrid nanofluid as a coolant and lubricant in heat engines,” *Applied Thermal Engineering*, vol. 102, pp. 45–54, 2016.
- [89] M. Gupta, V. Singh, R. Kumar, and Z. Said, “A review on thermophysical properties of nanofluids and heat transfer applications,” *Renewable and Sustainable Energy Reviews*, vol. 74, pp. 638–670, 2017.
- [90] M. H. Esfe, S. Saedodin, O. Mahian, and S. Wongwises, “Thermophysical properties, heat transfer and pressure drop of cooh-functionalized multi walled carbon nanotubes/water nanofluids,” *International Communications in Heat and Mass Transfer*, vol. 58, pp. 176–183, 2014.
- [91] S. Peyghambarzadeh, S. Hashemabadi, M. Naraki, and Y. Vermahmoudi, “Experimental study of overall heat transfer coefficient in the application of dilute nanofluids in the car radiator,” *Applied Thermal Engineering*, vol. 52, no. 1, pp. 8–16, 2013.

- [92] L. S. Sundar, K. Sharma, M. Naik, and M. K. Singh, “Empirical and theoretical correlations on viscosity of nanofluids: A review,” *Renewable and sustainable energy reviews*, vol. 25, pp. 670–686, 2013.
- [93] M. Naik and L. S. Sundar, “Investigation into thermophysical properties of glycol based cuo nanofluid for heat transfer applications,” *World Academy of Science, Engineering and Technology*, vol. 59, pp. 440–446, 2011.
- [94] M. Assael, I. Metaxa, J. Arvanitidis, D. Christofilos, and C. Lioutas, “Thermal conductivity enhancement in aqueous suspensions of carbon multi-walled and double-walled nanotubes in the presence of two different dispersants,” *International Journal of Thermophysics*, vol. 26, no. 3, pp. 647–664, 2005.
- [95] S. Choi, Z. Zhang, W. Yu, F. Lockwood, and E. Grulke, “Anomalous thermal conductivity enhancement in nanotube suspensions,” *Applied physics letters*, vol. 79, no. 14, pp. 2252–2254, 2001.
- [96] K. Zhao, W. Heinzl, M. Wenzel, S. Büttner, F. Bollen, G. Lange, S. Heinzl, and N. Sarda, “Experimental study of the memsys vacuum-multi-effect-membrane-distillation (v-memd) module,” *Desalination*, vol. 323, pp. 150–160, 2013.
- [97] J. Andrés-Mañas, A. Ruiz-Aguirre, F. Acién, and G. Zaragoza, “Performance increase of membrane distillation pilot scale modules operating in vacuum-enhanced air-gap configuration,” *Desalination*, vol. 475, p. 114 202, 2020.
- [98] S. Özerinç, S. Kakaç, and A. G. Yazıcıoğlu, “Enhanced thermal conductivity of nanofluids: A state-of-the-art review,” *Microfluidics and Nanofluidics*, vol. 8, no. 2, pp. 145–170, 2010.
- [99] J. A. Eastman, S. Choi, S. Li, W. Yu, and L. Thompson, “Anomalously increased effective thermal conductivities of ethylene glycol-based nanofluids containing copper nanoparticles,” *Applied physics letters*, vol. 78, no. 6, pp. 718–720, 2001.
- [100] M. Chopkar, P. K. Das, and I. Manna, “Synthesis and characterization of nanofluid for advanced heat transfer applications,” *Scripta Materialia*, vol. 55, no. 6, pp. 549–552, 2006.
- [101] Y. Feng, B. Yu, P. Xu, and M. Zou, “The effective thermal conductivity of nanofluids based on the nanolayer and the aggregation of nanoparticles,” *Journal of Physics D: Applied Physics*, vol. 40, no. 10, p. 3164, 2007.
- [102] R. Prasher, P. E. Phelan, and P. Bhattacharya, “Effect of aggregation kinetics on the thermal conductivity of nanoscale colloidal solutions (nanofluid),” *Nano letters*, vol. 6, no. 7, pp. 1529–1534, 2006.

- [103] D. Rouxel, R. Hadji, B. Vincent, Y. Fort, *et al.*, “Effect of ultrasonication and dispersion stability on the cluster size of alumina nanoscale particles in aqueous solutions,” *Ultrasonics sonochemistry*, vol. 18, no. 1, pp. 382–388, 2011.
- [104] N. Mandzy, E. Grulke, and T. Druffel, “Breakage of tio₂ agglomerates in electrostatically stabilized aqueous dispersions,” *Powder technology*, vol. 160, no. 2, pp. 121–126, 2005.
- [105] O. Vasylykiv and Y. Sakka, “Synthesis and colloidal processing of zirconia nanopowder,” *Journal of the American Ceramic Society*, vol. 84, no. 11, pp. 2489–2494, 2001.
- [106] P.-C. Ma, N. A. Siddiqui, G. Marom, and J.-K. Kim, “Dispersion and functionalization of carbon nanotubes for polymer-based nanocomposites: A review,” *Composites Part A: Applied Science and Manufacturing*, vol. 41, no. 10, pp. 1345–1367, 2010.
- [107] C. Boo, J. Lee, and M. Elimelech, “Engineering surface energy and nanostructure of microporous films for expanded membrane distillation applications,” *Environmental science & technology*, vol. 50, no. 15, pp. 8112–8119, 2016.
- [108] D. M. Warsinger, J. Swaminathan, E. Guillen-Burrieza, H. A. Arafat, *et al.*, “Scaling and fouling in membrane distillation for desalination applications: A review,” *Desalination*, vol. 356, pp. 294–313, 2015.
- [109] G. Naidu, S. Jeong, S. Vigneswaran, T.-M. Hwang, Y.-J. Choi, and S.-H. Kim, “A review on fouling of membrane distillation,” *Desalination and water treatment*, vol. 57, no. 22, pp. 10 052–10 076, 2016.
- [110] M. El-Bourawi, Z. Ding, R. Ma, and M. Khayet, “A framework for better understanding membrane distillation separation process,” *Journal of membrane science*, vol. 285, no. 1-2, pp. 4–29, 2006.
- [111] E. Drioli, A. Ali, and F. Macedonio, “Membrane distillation: Recent developments and perspectives,” *Desalination*, vol. 356, pp. 56–84, 2015.
- [112] A. M. Alklaibi and N. Lior, “Membrane-distillation desalination: Status and potential,” *Desalination*, vol. 171, no. 2, pp. 111–131, 2005.
- [113] A. S. Alsaadi, N. Ghaffour, J.-D. Li, S. Gray, L. Francis, H. Maab, and G. L. Amy, “Modeling of air-gap membrane distillation process: A theoretical and experimental study,” *Journal of membrane science*, vol. 445, pp. 53–65, 2013.
- [114] I. Janajreh, K. El Kadi, R. Hashaikheh, and R. Ahmed, “Numerical investigation of air gap membrane distillation (agmd): Seeking optimal performance,” *Desalination*, vol. 424, pp. 122–130, 2017.

- [115] R. W. Bonner III, “Correlation for dropwise condensation heat transfer: Water, organic fluids, and inclination,” *International Journal of Heat and Mass Transfer*, vol. 61, pp. 245–253, 2013.
- [116] J. B. Boreyko, Y. Zhao, and C.-H. Chen, “Planar jumping-drop thermal diodes,” *Applied Physics Letters*, vol. 99, no. 23, p. 234 105, 2011.
- [117] S. Daniel, M. K. Chaudhury, and J. C. Chen, “Fast drop movements resulting from the phase change on a gradient surface,” *Science*, vol. 291, no. 5504, pp. 633–636, 2001.
- [118] A. Ghosh, S. Beaini, B. J. Zhang, R. Ganguly, and C. M. Megaridis, “Enhancing dropwise condensation through bioinspired wettability patterning,” *Langmuir*, vol. 30, no. 43, pp. 13 103–13 115, 2014.
- [119] P. Zhang, Y. Maeda, F. Lv, Y. Takata, and D. Orejon, “Enhanced coalescence-induced droplet-jumping on nanostructured superhydrophobic surfaces in the absence of microstructures,” *ACS applied materials & interfaces*, vol. 9, no. 40, pp. 35 391–35 403, 2017.
- [120] D. E. Kim, H. S. Ahn, and T.-S. Kwon, “Experimental investigation of filmwise and dropwise condensation inside transparent circular tubes,” *Applied Thermal Engineering*, vol. 110, pp. 412–423, 2017.
- [121] D. Attinger, C. Frankiewicz, A. R. Betz, T. M. Schutzius, R. Ganguly, A. Das, C.-J. Kim, and C. M. Megaridis, “Surface engineering for phase change heat transfer: A review,” *MRS Energy & Sustainability*, vol. 1, 2014.
- [122] P. S. Mahapatra, A. Ghosh, R. Ganguly, and C. M. Megaridis, “Key design and operating parameters for enhancing dropwise condensation through wettability patterning,” *International journal of heat and mass transfer*, vol. 92, pp. 877–883, 2016.
- [123] S. T. W. Kuruneru, K. Vafai, E. Sauret, and Y. Gu, “Application of porous metal foam heat exchangers and the implications of particulate fouling for energy-intensive industries,” *Chemical Engineering Science*, p. 115 968, 2020.
- [124] N. Dukhan and K.-C. Chen, “Heat transfer measurements in metal foam subjected to constant heat flux,” *Experimental Thermal and Fluid Science*, vol. 32, no. 2, pp. 624–631, 2007.
- [125] H. Huisseune, S. De Schampheleire, B. Ameel, and M. De Paepe, “Comparison of metal foam heat exchangers to a finned heat exchanger for low reynolds number applications,” *International Journal of Heat and Mass Transfer*, vol. 89, pp. 1–9, 2015.

- [126] A. Chumpia and K. Hooman, “Performance evaluation of single tubular aluminium foam heat exchangers,” *Applied Thermal Engineering*, vol. 66, no. 1-2, pp. 266–273, 2014.
- [127] D. P. Haack, K. R. Butcher, T. Kim, and T. Lu, “Novel lightweight metal foam heat exchangers,” in *2001 ASME Congress Proceedings*, 2001, pp. 1–7.
- [128] G. B. Abadi and K. C. Kim, “Experimental heat transfer and pressure drop in a metal-foam-filled tube heat exchanger,” *Experimental Thermal and Fluid Science*, vol. 82, pp. 42–49, 2017.
- [129] Y. Shouguang, D. Jiangwei, S. Dong, L. Sheng, and L. Jian, “Experimental investigation on the heat transfer performance of heat pipes with porous copper foam wicks,” *Materials Research Innovations*, vol. 19, no. sup5, S5–617, 2015.
- [130] C. Shum, G. Rosengarten, and Y. Zhu, “Enhancing wicking microflows in metallic foams,” *Microfluidics and Nanofluidics*, vol. 21, no. 12, p. 177, 2017.
- [131] X. Chang, N. Watanabe, and H. Nagano, “Visualization study of a loop heat pipe with two evaporators and one condenser under gravity-assisted condition,” *International Journal of Heat and Mass Transfer*, vol. 135, pp. 378–391, 2019.
- [132] A. R. Abd Elbar and H. Hassan, “Enhancement of hybrid solar desalination system composed of solar panel and solar still by using porous material and saline water pre-heating,” *Solar Energy*, vol. 204, pp. 382–394, 2020.
- [133] H. Hassan, M. S. Yousef, M. S. Ahmed, and M. Fathy, “Energy, exergy, environmental, and economic analysis of natural and forced cooling of solar still with porous media,” *Environmental Science and Pollution Research*, vol. 27, no. 30, pp. 38 221–38 240, 2020.
- [134] A. Volkov, E. Novitsky, I. Borisov, V. Vasilevsky, and V. Volkov, “Porous condenser for thermally driven membrane processes: Gravity-independent operation,” *Separation and Purification Technology*, vol. 171, pp. 191–196, 2016.
- [135] M. Khayet, “Membranes and theoretical modeling of membrane distillation: A review,” *Advances in colloid and interface science*, vol. 164, no. 1-2, pp. 56–88, 2011.
- [136] I. Hitsov, T. Maere, K. De Sitter, C. Dotremont, and I. Nopens, “Modelling approaches in membrane distillation: A critical review,” *Separation and Purification Technology*, vol. 142, pp. 48–64, 2015.
- [137] F. Laganà, G. Barbieri, and E. Drioli, “Direct contact membrane distillation: Modelling and concentration experiments,” *Journal of Membrane Science*, vol. 166, no. 1, pp. 1–11, 2000.

- [138] V. A. Bui, L. T. Vu, and M. H. Nguyen, “Simulation and optimisation of direct contact membrane distillation for energy efficiency,” *Desalination*, vol. 259, no. 1-3, pp. 29–37, 2010.
- [139] M. N. Chernyshov, G. W. Meindersma, and A. B. de Haan, “Modelling temperature and salt concentration distribution in membrane distillation feed channel,” *Desalination*, vol. 157, no. 1-3, pp. 315–324, 2003.
- [140] D. J. Preston, K. L. Wilke, Z. Lu, S. S. Cruz, Y. Zhao, L. L. Becerra, and E. N. Wang, “Gravitationally driven wicking for enhanced condensation heat transfer,” *Langmuir*, vol. 34, no. 15, pp. 4658–4664, 2018.
- [141] K. W. Lawson and D. R. Lloyd, “Membrane distillation. i. module design and performance evaluation using vacuum membrane distillation,” *Journal of membrane science*, vol. 120, no. 1, pp. 111–121, 1996.
- [142] S. Bandini, A. Saavedra, and G. C. Sarti, “Vacuum membrane distillation: Experiments and modeling,” *AIChE Journal*, vol. 43, no. 2, pp. 398–408, 1997.
- [143] M. A. E.-R. Abu-Zeid, Y. Zhang, H. Dong, L. Zhang, H.-L. Chen, and L. Hou, “A comprehensive review of vacuum membrane distillation technique,” *Desalination*, vol. 356, pp. 1–14, 2015.
- [144] J. Mengual, M. Khayet, and M. Godino, “Heat and mass transfer in vacuum membrane distillation,” *International Journal of Heat and Mass Transfer*, vol. 47, no. 4, pp. 865–875, 2004.
- [145] H. W. Chung, J. Swaminathan, D. M. Warsinger, *et al.*, “Multistage vacuum membrane distillation (msvmd) systems for high salinity applications,” *Journal of Membrane Science*, vol. 497, pp. 128–141, 2016.
- [146] A. S. Alsaadi, L. Francis, H. Maab, G. L. Amy, and N. Ghaffour, “Evaluation of air gap membrane distillation process running under sub-atmospheric conditions: Experimental and simulation studies,” *Journal of Membrane Science*, vol. 489, pp. 73–80, 2015.
- [147] Z. Liu, Q. Gao, X. Lu, Z. Ma, H. Zhang, and C. Wu, “Experimental study of the optimal vacuum pressure in vacuum assisted air gap membrane distillation process,” *Desalination*, vol. 414, pp. 63–72, 2017.

A. NANOFUID MODEL SYSTEM PARAMETERS

Table A.1. System parameters used in the numerical model for nanofluids in membrane distillation

Parameter	Symbol	Value	Units
Membrane permeability coefficient	B_o	$2 * 10^{-10}$	s
Membrane thickness	δ_m	200	μm
Membrane porosity	ϕ	0.8	-
Membrane thermal conductivity	k_m	0.2	W/m K
Membrane width per unit flow rate	$w/\dot{m}_{f,in}$	12	m/(kg/s)
Module length	L	6	m
Top temperature	$T_{f,in}$	85	$^{\circ}\text{C}$
Seawater inlet temperature	$T_{sw,in}$	25	$^{\circ}\text{C}$
Channel height	d_{ch}	1	mm
Feed inlet salinity	Sal_{in}	35	g/kg
Gap thickness	d_{gap}	1	mm
Gap conductivity (CGMD)	k_{gap}	10	W/m K
Gap conductivity (PGMD)	k_{gap}	0.668	W/m K
Gap spacer conductivity (AGMD)	$k_{gap,spacer}$	0.2	W/m K
Specific heat capacity (copper oxide)	$c_{p,CuO}$	531	J/kg K
Density of copper oxide	ρ_{CuO}	6310	kg/m ³
Thermal conductivity of copper oxide	$k_{p,CuO}$	76.5	W/m K
Average particle diameter (CuO)	$D_{p,CuO}$	29	nm
Diffusivity of salt in water	$D_{s,w}$	$1.76 * 10^{-9}$	m ² /s

B. SLIPS MODEL SYSTEM PARAMETERS

Table B.1. System parameters used in the numerical model for SLIPS in membrane distillation

Parameter	Symbol	Value	Units
Membrane permeability coefficient	B_o	$2 * 10^{-10}$	s
Membrane thickness	δ_m	200	μm
Membrane porosity	ϕ	0.8	-
Membrane thermal conductivity	k_m	0.2	W/m K
Membrane width per unit flow rate	$w/\dot{m}_{f,in}$	12	m/(kg/s)
Module length	L	6	m
Top temperature	$T_{f,in}$	85	$^{\circ}\text{C}$
Seawater inlet temperature	$T_{sw,in}$	25	$^{\circ}\text{C}$
Channel height	d_{ch}	1	mm
Feed inlet salinity	Sal_{in}	35	g/kg
Gap thickness	d_{gap}	0.1	mm
Gap conductivity (CGMD)	k_{gap}	10	W/m K
Gap conductivity (PGMD)	k_{gap}	0.668	W/m K
Gap spacer conductivity (AGMD)	$k_{gap,spacer}$	0.2	W/m K
Diffusivity of salt in water	$D_{s,w}$	$1.76 * 10^{-9}$	m^2/s

C. POROUS CONDENSER MODEL SYSTEM PARAMETERS

Table C.1. System parameters used in the numerical model for porous condensers in membrane distillation

Parameter	Symbol	Value	Units
Membrane permeability coefficient	B_o	$2 * 10^{-10}$	s
Membrane thickness	δ_m	200	μm
Membrane porosity	ϕ	0.8	-
Membrane thermal conductivity	k_m	0.2	W/m K
Membrane width per unit flow rate	$w/\dot{m}_{f,in}$	12	m/(kg/s)
Module length	L	6	m
Top temperature	$T_{f,in}$	85	$^{\circ}\text{C}$
Seawater inlet temperature	$T_{sw,in}$	25	$^{\circ}\text{C}$
Channel height	d_{ch}	1	mm
Feed inlet salinity	Sal_{in}	35	g/kg
Gap thickness	d_{gap}	0.1	mm
Gap conductivity (CGMD)	k_{gap}	10	W/m K
Gap conductivity (PGMD)	k_{gap}	0.668	W/m K
Gap spacer conductivity (AGMD)	$k_{gap,spacer}$	0.2	W/m K
Porous condenser thickness	δ_c	3	mm
Condenser permeability	κ	$1.25 * 10^{-9}$	m^2
Wick thermal conductivity	k_{wick}	14.7	W/m K
Diffusivity of salt in water	$D_{s,w}$	$1.76 * 10^{-9}$	m^2/s